

DVB-S2 modem algorithms design and performance over typical satellite channels

E. Casini, R. De Gaudenzi^{*,†} and A. Ginesi

*European Space Agency (ESA), European Space and Technology Centre (ESTEC), Keplerlaan 1,
2200 AG Noordwijk, The Netherlands*

SUMMARY

In this paper we propose a design of the main modulation and demodulation units of a modem compliant with the new DVB-S2 standard (*Int. J. Satellite Commun.* 2004; **22**:249–268). A typical satellite channel model consistent with the targeted applications of the aforementioned standard is assumed. In particular, non-linear pre-compensation as well as synchronization techniques are described in detail and their performance assessed by means of analysis and computer simulations. The proposed algorithms are shown to provide a good trade-off between complexity and performance and they apply to both the broadcast and the unicast profiles, the latter allowing the exploitation of adaptive coding and modulation (ACM) (Proceedings of the 20th AIAA Satellite Communication Systems Conference, Montreal, AIAA-paper 2002-1863, May 2002). Finally, end-to-end system performances in term of BER versus the signal-to-noise ratio are shown as a result of extensive computer simulations. The whole communication chain is modelled in these simulations, including the BCH and LDPC coder, the modulator with the pre-distortion techniques, the satellite transponder model with its typical impairments, the downlink chain inclusive of the RF-front-end phase noise, the demodulator with the synchronization sub-system units and finally the LDPC and BCH decoders. Copyright © 2004 John Wiley & Sons, Ltd.

KEY WORDS: broadband communications; digital pre-distortion; nonlinear satellite channels; satellite digital broadcasting; synchronization

1. INTRODUCTION

One of the key features of the new DVB-S2 standard [1] is represented by the extended range of spectral efficiencies supported combined with near Shannon power and spectral efficiency. These physical layer excellent performances are combined with the truly remarkable on-the-fly frame-by-frame reconfigurability. This capability is particularly suited to economically support new consumer multimedia interactive services exploiting the unicast profile with adaptive coding and modulation (ACM) [2, 3]. The DVB-S2 standard has been designed having in mind the peculiarities of the satellite channel, in particular the on-board satellite linear and non-linear distortions, the link fading impairments and the carrier phase noise dominated by the

*Correspondence to: Riccardo De Gaudenzi, European Space Agency, Keplerlaan 1, 2200 AG Noordwijk, The Netherlands.

† E-mail: rdegaude@xrsun0.estec.esa.nl

user terminal RF front-end. It is then evident the interest to complement the outstanding DVB-S2 coded modulation performance results over additive white Gaussian noise (AWGN) presented in the companion paper [4] by extensive end-to-end performance assessment over typical satellite channels.

It is well known from literature [5] that satellite linear and non-linear distortions combined with the user terminal radio frequency (RF) front-end phase noise contributions can cause important link performance impairments. The DVB-S2 adoption of high-order modulation formats (up to 32-ary APSK) makes the potential channel impairments much more important than those encountered by the classical QPSK modulation format adopted by the former DVB-S standard [6]. In this paper the issue of proper modulator and demodulator system design to minimize the end-to-end link losses is also tackled for the reference satellite channel characteristics that were defined by the DVB-S2 technical group. In particular, we show that by proper digital signal processing algorithm design on both the modulator and the demodulator side it is possible to keep non-ideal satellite channel induced losses within acceptable limits. We will also demonstrate that, thanks to the constellation design and digital pre-distortion techniques, we can optimally drive the satellite non-linear travelling wave tube amplifier (TWTA) in saturation (maximum DC power conversion efficiency) for QPSK, 8PSK and 16APSK. The working point for 32APSK has also been optimized for the minimum overall loss.

One of the most challenging issues that one has to deal with when designing a DVB-S2 demodulator is the carrier synchronization strategy. As it is known, in broadband satellite transmissions, the phase of the carrier is usually affected by a number of distortions which comprise: (i) semi-static channel phase rotations due to delay and/or the presence of transmit (TX), satellite non-linear transponder and receive (RX) conditioning filters, (ii) slowly varying phase rotations due to channel fading and (iii) TX and RX oscillator phase and phase noise. A number of algorithms are available in literature to address the issue of carrier phase recovery (see Reference [7] for a comprehensive literature review) for different modulation schemes. However, the exploitation of high-order modulations combined with near-Shannon coding techniques, calls for devising carrier phase estimation techniques capable to operate at low SNR and with various modulation formats. Also, the desire to use low cost commercial low noise blocks (LNBs) and tuners leads to a remarkable increase of the carrier phase noise which the system has to be able to tolerate making conventional carrier phase estimators suffering from an unacceptable cycle slip rate.

In those circumstances the use of pilot-aided (PA) schemes is often the only viable solution to the problem. In these schemes, a certain amount of pilot (known) symbols are interleaved with the data streams, in order to help the channel estimation process. Pilot symbols are then discarded before the decoder. DVB-S2 allows inserting pilot fields in both the broadcast and unicast profile. Simple digital signal processing techniques able to exploit the pilot fields and the modulated symbols (when required) are investigated and shown to provide good tracking performance also over the worst-case channel conditions.

The rest of the paper is organized as follows: Section 2 describes the adopted system model, Section 3 deals with the modulator and demodulator algorithmic design, Section 4 reports the key performance simulation results. Finally, Section 5 summarizes the paper findings and outlines future work directions.

2. SYSTEM MODEL

In the following we detail the system model that we adopted for the end-to-end DVB-S2 system analysis. Compared to the full standard described in this very same journal issue [1], we represent in our simulator all key aspects impacting the physical layer performance. Possible simplifications not affecting the fidelity of the simulator are introduced and justified when required. The high-level system block diagram considered is shown in Figure 1. The first block in the chain is the gateway modulator which is described in detail in Section 2.1. The RF output signal is then uplinked to the satellite through the feeder link. Although in general the uplink noise contribution at the satellite input is not negligible, the DVB-S2 working group agreed assuming that the downlink noise dominates the overall link thermal noise contributions to limit the number of cases to be simulated. The satellite transponder details are discussed in Section 2.2. Basically for our purposes it performs input signal filtering, frequency translation and high-

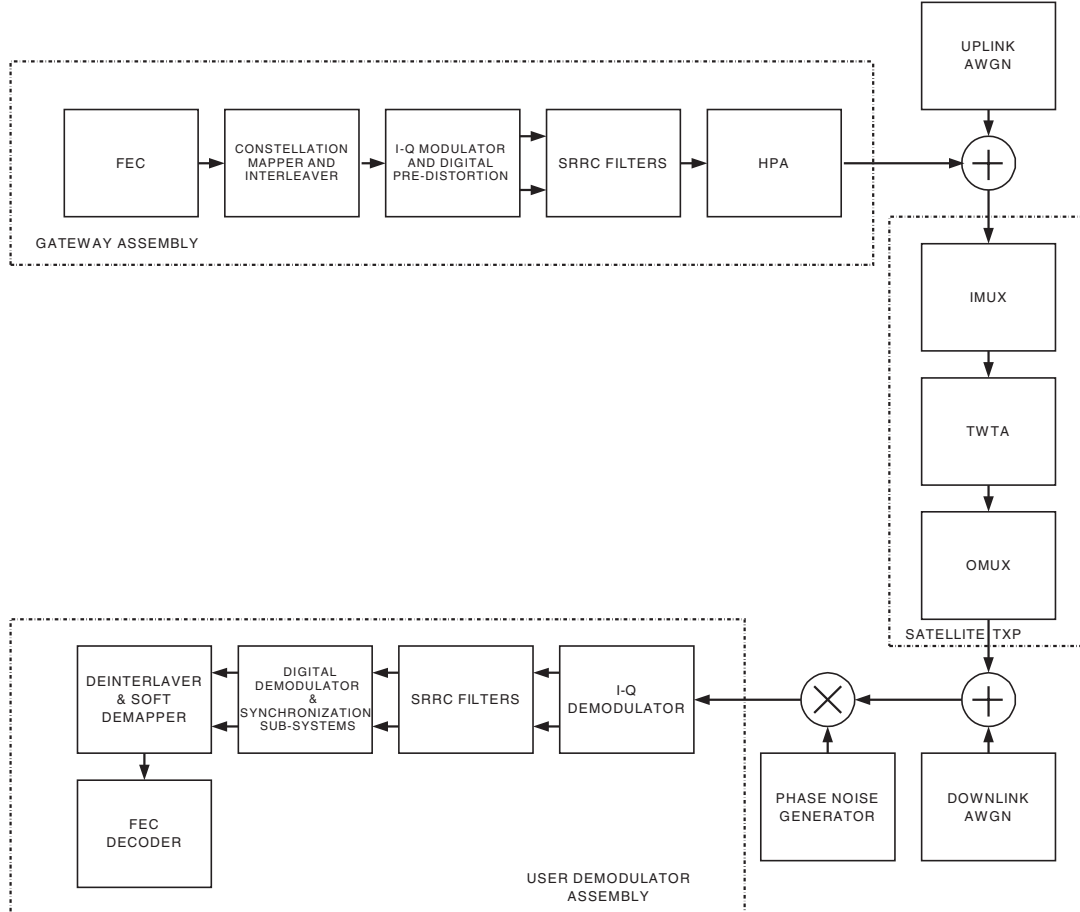


Figure 1. High-level DVB-S2 system model.

power amplification followed by output filtering. The forward downlink channel discussed in Section 2.3 is representative of the satellite to user terminal link and is simply characterized by the AWGN and the receiver RF front-end phase noise. Finally, baseband signal demodulation and decoding are detailed in Section 2.4.

2.1. Modulator and uplink channel

The modulator model does not include the Mode Adaptation and Stream Adaptation subsystem which is discussed in detail in References [1, 2]. Those functional blocks do not have impact on the physical layer performance and are therefore not considered here. So information bits generated by a binary random generator enter directly the FEC Encoding block composed by an outer BCH code and an inner LDPC code operating on K_{BCH} input information bit block whose detailed description is contained in Reference [4]. Binary coded bits in a block of size of n_{LDPC} bits are then row-by-column interleaved (except for the QPSK case) before being Gray-mapped onto the five possible M -ary constellations. The constellation points are contained in a look-up table which may include pre-compensation of the band-limited non-linear satellite channel effects. Details of the pre-compensation techniques are provided in Section 3.1. Payload (PL) signalling and pilot insertion in the so-called PL Frame [1] follows. For our purposes however we limit to the pilot insertion as the PL signalling is not relevant. The physical layer binary scrambler is then applied to the I-Q branches. Baseband square-root raised cosine (SRRC) filtering is then applied before the I-Q carrier modulation.

The forward feeder link is in general modelled by a non-linear high-power amplifier (HPA) and an AWGN uplink generator. For DVB-S2 evaluation it was decided to do not consider these effects.

2.2. Satellite transponder

Within the DVB-S2 group a transparent satellite transponder has been assumed for the end-to-end channel simulator. The transponder model is composed of an input demultiplexer (IMUX) filter, a TWTA and an output multiplexer filter (OMUX). Low noise amplifier is assumed ideal except for its noise contribution which is incorporated in the uplink AWGN generator. Also satellite transponder down and upconverters are considered to be ideal. For the IMUX and OMUX modelling whose measured characteristics are reported in Figures 2–5 a FIR model has been synthesized approximating the measured filter characteristic both in amplitude and group delay. The group delay matching was mainly limited to the in-band filter region. The simulated IMUX characteristic is shown in Figures 2 and 3 where it is evident the fairly good match between the measured response and the synthesized model, although the resulting FIR filter complexity is not negligible (300 taps). A similar approach has been followed for the OMUX model. Measured versus simulated OMUX characteristics are reported in Figures 4 and 5, respectively. In this case the FIR filter size amounts to 200 taps.

Concerning the satellite TWTA HPA, the non-linearized amplifier defined by the DVB-S2 committee has been adopted. Experimental AM/AM and AM/PM characteristic points have been interpolated through a memory-less spline function and the corresponding characteristic is shown in Figures 6 and 7. Linear extrapolation has been used for points exceeding the available sets of points. As it is common practice, the zero dB input back-off (IBO) point has been set to the AM/AM characteristic point corresponding to the peak power of the tube.

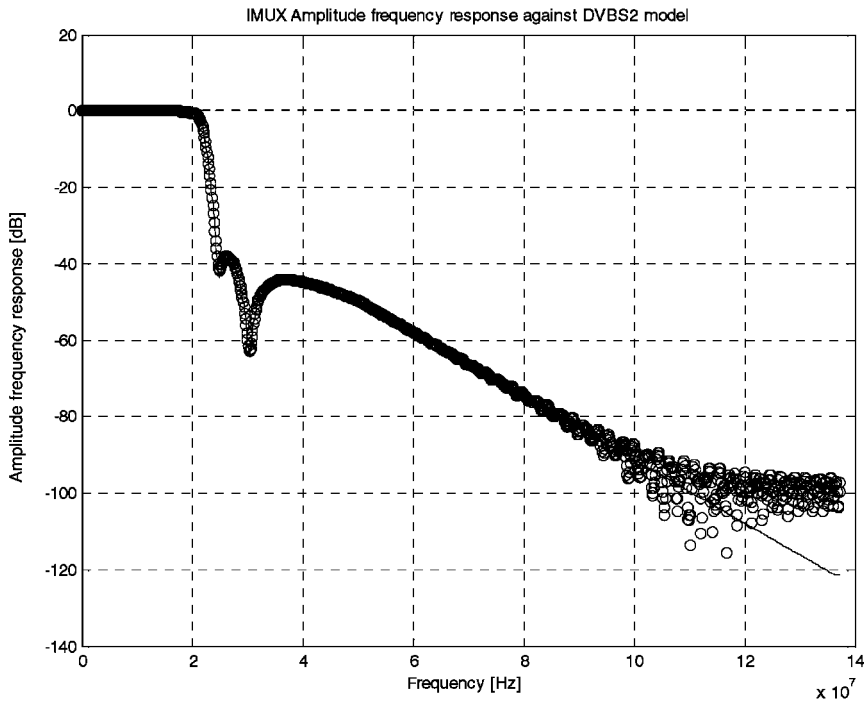


Figure 2. IMUX characteristic measured (blue line) and simulated (red circles): amplitude response.

2.3. Downlink channel

The downlink satellite channel comprises several impairments resulting in signal attenuation (signal fading due to rain, scintillations, atmospheric gas absorption, etc.). However, as far as static performance analysis is concerned, these effects can be modelled with a constant attenuation which in turns can be taken into account within the signal E_s/N_0 at the demodulator input and thus these phenomena result to be completely transparent to our analysis.

The other impairments that are modelled within the downlink channel mostly pertain to the terminal receiver like clock and carrier frequency errors as well as carrier phase noise. Clock frequency errors are due to long term instabilities of the terminal oscillator which provides the terminal demodulator sampling clock, while Doppler effects due to the GEO satellite movements are usually negligible. The precision of the oscillator depends on its quality (i.e. its cost) but usually it can be considered to be limited to a maximum of 10 ppm. Carrier frequency errors can be attributed to several factors, but the main contributors are the terminal LNB oscillator instabilities and Doppler effects. Within DVB-S2 a maximum carrier frequency error of 5 MHz has been specified for consumer-type of terminal receivers. However, the residual differential frequency errors when tuning to a different downlink carrier can be considered much smaller, i.e. in the order of max 100 kHz.

The main contributor to the carrier phase noise is the terminal LNB RF oscillator, especially in low-cost equipments. The terminal tuner contribution has a lower impact but it is not

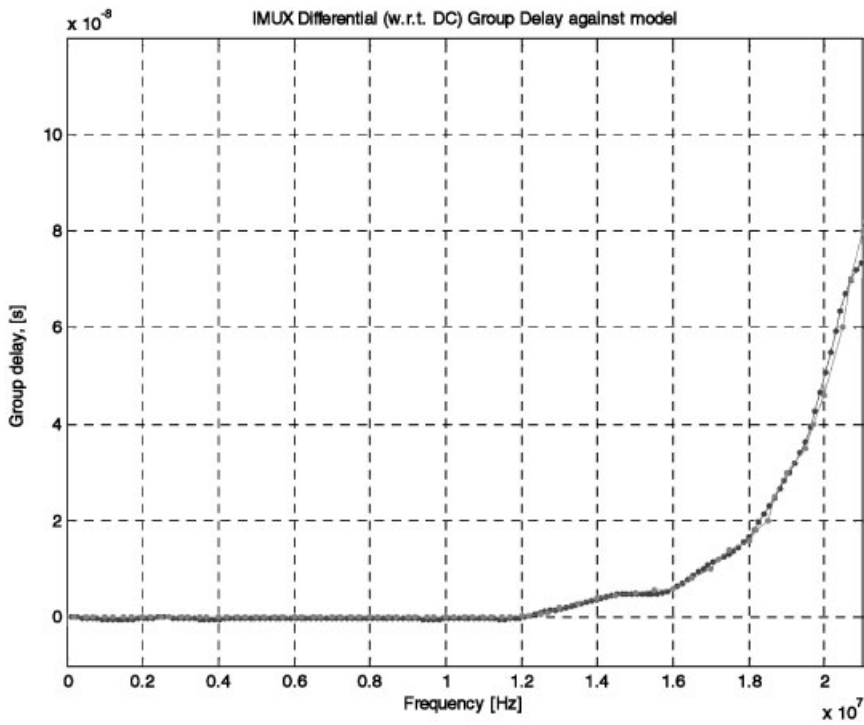


Figure 3. IMUX characteristic measured (red dotted line) and simulated (blue dotted line): group delay response.

completely negligible. The worst case power spectral density (PSD) of the combined phase noise contribution of terminal satellite receivers' tuners and LNBs has been specified by DVB-S2 and is sketched in Figure 8. Although our analysis is focused on this particular phase noise PSD, it is clear that the algorithms presented can easily be ported to work with other phase noise's PSDs. To be remarked that the PSD depicted in Figure 8 represents the single side band (SSB) PSD of the carrier with phase noise which can also be shown to correspond to the double side band (DSB) of the phase noise multiplicative process, under the assumption of small signals.

For the time domain simulations that have been carried out, a time domain synthesis of the phase noise samples is required. To this purpose, a time domain synthetic model has been generated and its description is reported in the following. Since it is expected that the phase noise will only affect the phase recovery scheme and this latter works entirely at the symbol rate, the discrete phase noise process that will be synthesized is made up by the phase noise samples at symbol rate at the symbol matched filter (MF) output. This simplification allows to considerably speeding up the simulation time, as well as simplifies the synthesis process. Two digital filters have been designed whose combined frequency response matches the target phase noise mask for the symbol rate value of 25 Mbaud. The approach that has been used is the least square error fit of the IIR filter amplitude frequency response to the target mask. Also, in order to better match the phase noise PSD below 1 kHz, an '*ad hoc*' design filter has also been added in parallel (see Figure 9).

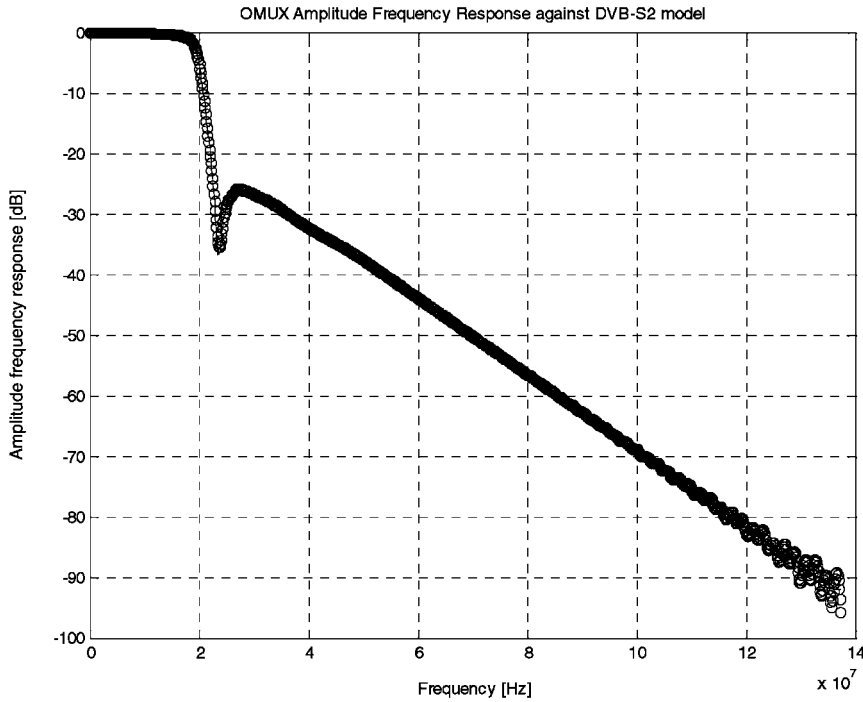


Figure 4. OMUX characteristic measured (blue line) and simulated (red circles): amplitude response.

The filters $H_1(z)$ and $H_2(z)$ have transfer functions,

$$H_1(z) = \frac{-4.7 \times 10^{-11}}{(z - 0.999975)^2} \quad (1)$$

$$H_2(z) = \frac{2.8 \times 10^{-6}(z - 1.103181)(z - 0.992015)}{(z - 0.991725)(z - 0.9999985)(z - 0.563507)} \quad (2)$$

As Figure 10 shows, there is a fairly good match between the measured PSD of the synthesized phase noise and the target PSD mask. The output of the phase noise emulator of Figure 9 modulates a complex phasor which, in turn, multiplies the received signal (see Figure 1).

2.4. Demodulator

The architecture of a demodulator compliant with the DVB-S2 standard comprises of an RF/IF part whose architecture depends on the RF frequency band used by the application (Ku versus Ka) as well as to whether low cost user equipments or professional equipments are used. Also, a number of choices can be made on the down-conversion strategy. For example, in low cost DTH terminals usually the RF received signal is first down-converted to a intermediate frequency by a LNB that is placed in the proximity of the antenna feeder, then the signal is further down-shifted in frequency by a tuner, which usually, in low rate equipments, directly converts the signal to complex-baseband. A couple of well matched A/D converters sample the

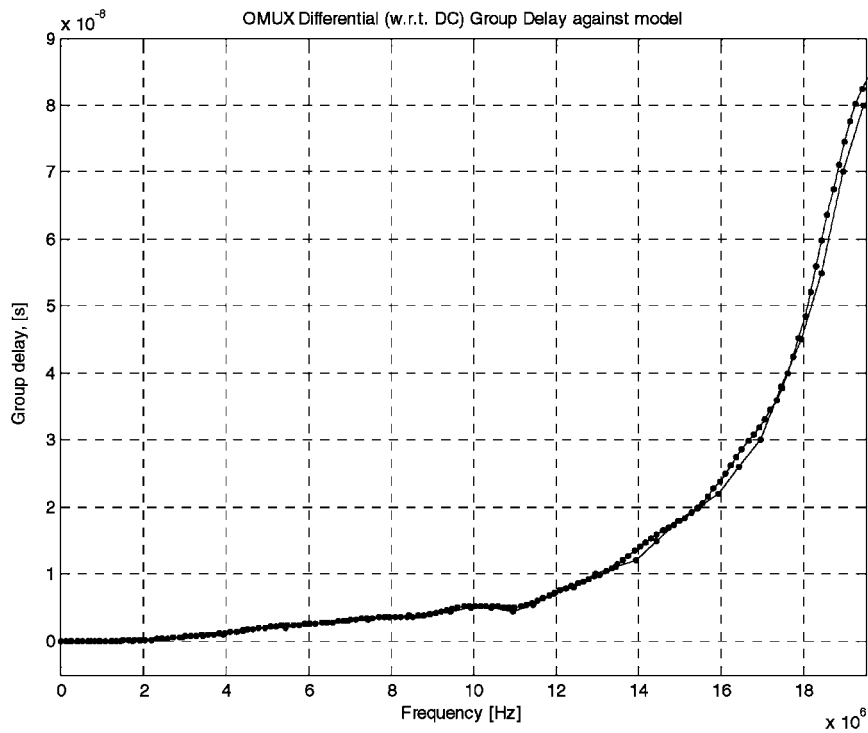


Figure 5. OMUX characteristic measured (red dotted line) and simulated (blue dotted line): group delay response.

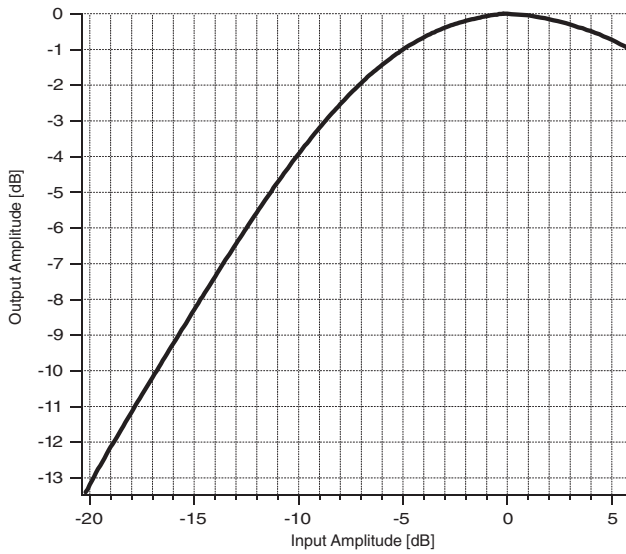


Figure 6. Satellite TWTA characteristics: AM/AM.

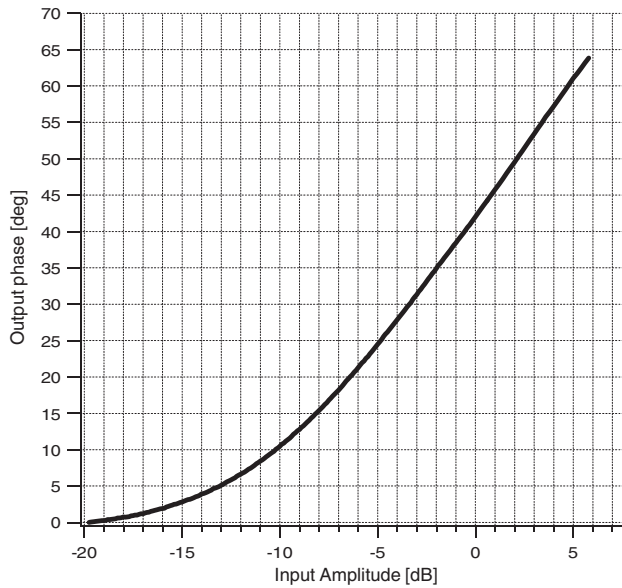


Figure 7. Satellite TWTA characteristics: AM/PM.

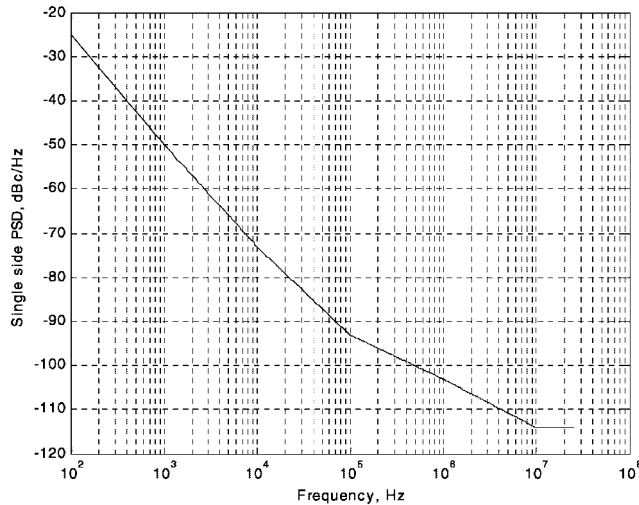


Figure 8. Aggregate DVB-S2 phase noise mask for LNB + tuner.

signal and feed the digital demodulator section of the receiver. The block diagram of the digital demodulator is shown in Figure 11. It is assumed that the signal from the RF/IF front end is down-converted to baseband so that the two I-Q components are made available to the digital demodulator input, sampled at a rate high enough to avoid signal aliasing.

A number of synchronization sub-systems are present in the demodulator in order to coherently demodulate the received signal. They will be described in details in the next sections

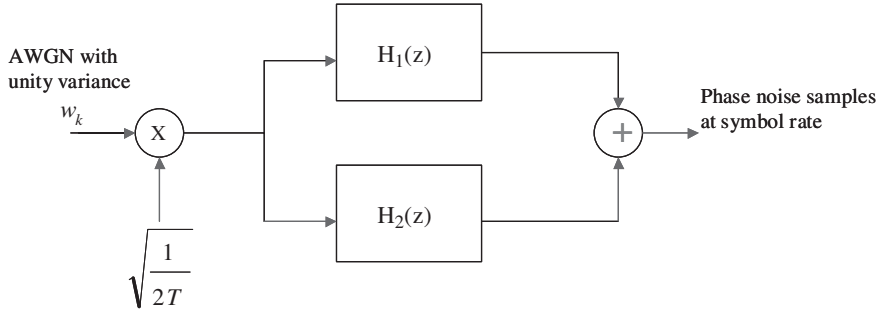


Figure 9. Synthesis of the phase noise process.

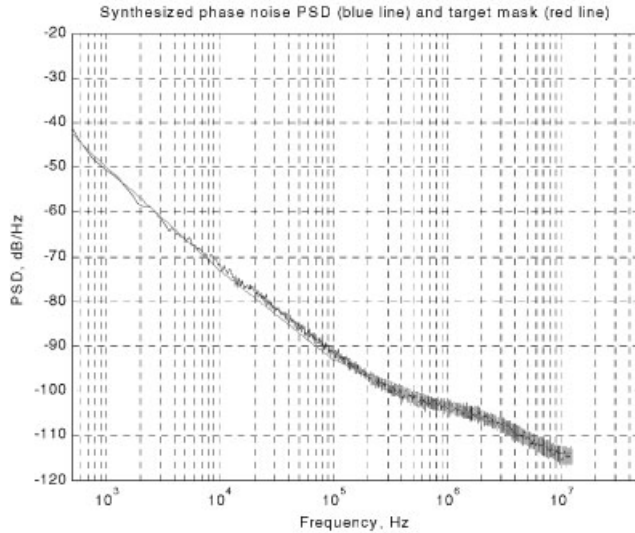


Figure 10. Synthesized phase noise PSD compared to the target for 25 Mbaud symbol rate.

but here a general overview is given. The first correction the signal receives is about the carrier frequency. The coarse frequency correction unit provides a first correction with an all-digital second-order frequency loop. The target is for a lock-in range of up to 5 MHz, which corresponds to half the minimum hypothesized symbol rate of 10 Mbaud. Then, the next block deals with clock recovery whose timing adjustment is carried out through a digital interpolator. Typically, this latter can be implemented as a parabolic or cubic interpolator (4 taps) in order to limit the distortions to the minimum. Matched filtering follows, at two samples per symbol. The number of taps of this filter depends on the roll-off factor. In our simulations we assumed an impulse response that spans 20 symbol periods with no particular optimization. As we will see that leads to a performance degradation of less than 0.1 dB. Then, two distinct feedforward units perform fine frequency and phase compensation. Digital automatic gain control (DAGC) is then performed in order to adjust the level of the incoming symbols to the reference constellation and further carrier phase adjustment is carried out by a DPLL. The de-rotated symbols are finally passed to the decoder where the pilot symbols are first discarded and the channel intrinsics are computed on the data symbols.

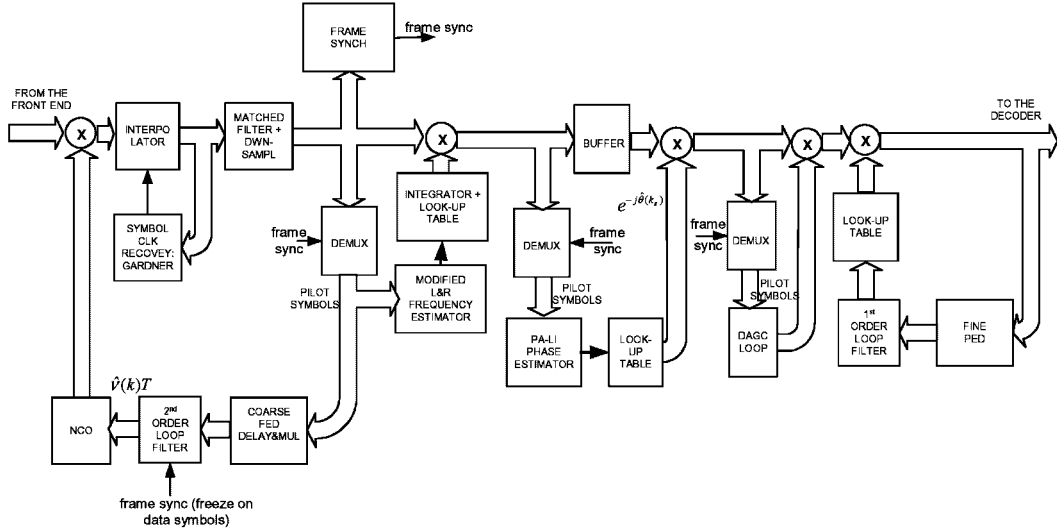


Figure 11. Block diagram of the DVB-S2 digital demodulator.

All the synchronization units are fully PA, i.e. do not make any use of the data symbols, except for the clock recovery, the frame synchronizer and the last DPLL. This latter works on the data symbols only and its presence is required to lower the phase error RMS for high-order constellations (16 and 32-APSK). The frame synchronizer uses a unique word correlator that works on symbol-by-symbol basis and feeds with its final frame alignment the two demultiplexer of the demodulator.

During initial acquisition the synchronization tasks are performed with the following order:

- (i) Clock recovery is activated first; in fact the Gardner algorithm can work with relatively large frequency errors.
- (ii) Once the clock recovery has converged, frame synchronization can be carried out using techniques that are relatively insensitive to the maximum specified carrier frequency error.
- (iii) Coarse and fine carrier frequency is then carried out.
- (iv) Finally, phase recovery is performed.

More details on the acquisition procedure are given to the synchronization sub-system sections. However, to summarize we can say that the requirement of 100 ms acquisition time for channel zapping can be met down to QPSK $\frac{1}{2}$. For lower code rates, a slightly longer convergence time is required.

3. MODEM ALGORITHMS

In this section we describe the most important algorithms for a DVB-S2 modem, from signal pre-distortion techniques to combat the channel non-linear effects, to the clock and carrier synchronization algorithms and finally the digital AGC algorithm.

Throughout the section we use the following notation: $z(k)$ are the samples at the signal matched filter output (SMF), $z^P(k)$'s are the $z(k)$ samples which refer to pilot symbol location within the DVB-S2 physical layer frame, $c(k)$'s are the complex information data symbols belonging to a QPSK, 8PSK, 16APSK or 32APSK constellation, $c^P(k)$'s are the pilot symbols and L_s is the pilot symbols periodicity in number of symbols. We also recall that DVB-S2 allows for inserting pilot fields of $L_p = 36$ symbols every 16 slots, i.e. $L_s = 1476$ symbols in both the broadcast and unicast profile [8]. Those values were optimized for 8PSK $r = \frac{2}{3}$ physical layer configuration.

3.1. Modulator with pre-distortion

The selected APSK modulation for DVB-S2 is characterized by the fact that constellation points lie on concentric circles. This circular symmetry is particularly suited to non-linear amplification as it is easier to maintain the APSK circular constellation shape over a non-linear HPA than for classical squared QAM constellations. In Reference [9], it has been shown that by proper APSK constellation parameters optimization it is possible to achieve performance that is very close or even slightly superior to QAM over AWGN channels. PSK modulation formats (QPSK and 8PSK) result to be a particular case of APSK corresponding to the case when the points are all lying on a single circumference. For 16APSK two rings of points are present with 4 points on the inner ring and 12 points on the outer ring. In the case of 32APSK three rings are present with 4 points on the inner ring, 12 points on the middle ring and 16 points on the outer ring. Over non-linear channels the APSK constellation, when observed at the demodulator symbol matched filter decimated output, is affected by two main kinds of impairment:

1. The constellation centroids[‡] warping due to the AM/AM and AM/PM HPA non-linear characteristic.
2. The clustering effect due to the inter-symbol interference (ISI) experienced at the demodulator matched filter output.

The warping phenomenon is responsible for the reduction of the distance among APSK rings (AM/AM compression) as well as a differential phase rotation among them (AM/PM differential phase). The ISI causing the constellation clustering is related to the demodulator SRRC filter (SRRCf) mismatch on the received signal due to the combination of the signal band limiting introducing memory in the channel, the IMUX filter linear distortion, the HPA memoryless non-linearity, the OMUX linear filter distortions, resulting in a non-linear channel with memory. These effects can be easily understood recalling the TWTA AM/AM and AM/PM characteristic and by observing the pictorial representation of Figure 12.

Clearly the warping effect has no impact on single ring constellations such as QPSK and 8PSK[§] but is causing important degradations for 16APSK and 32APSK. This is because the decoder log-likelihood ratios are typically computed using the 'standard' APSK constellation and do not take into account the centroid locations distortion caused by the HPA. A possible solution to the problem was introduced in Reference [10]. The idea is to replace the decoder

[‡]By centroid we consider the compilation of received constellation cluster centre of mass conditioned to each constellation point.

[§]The phase and amplitude PSK distortion will be compensated for by the demodulator AGC and phase recovery subsystems.

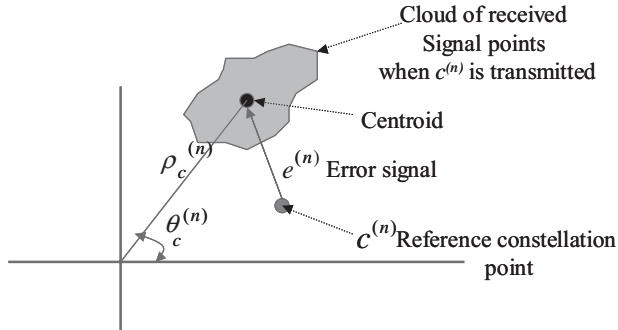


Figure 12. Pictorial view of the static pre-distortion algorithm.

reference constellation points with the distorted constellation centroids observed at the SMF output. In this way the majority of the warping distortion impairments can be recovered at the decoder side with no need for pre-distortion at the modulator. However, this technique requires decoder customization to a specific non-linear channel thus it cannot be accepted for consumer applications. In Reference [12] two kinds of pre-distortion techniques have been considered for APSK: ‘static’ and ‘dynamic’. The static pre-distortion technique simply consists in modifying the APSK constellation points to minimize the demodulator SMF samples centroids distance from the ‘wanted’ reference constellation. The static pre-compensation is preferably performed off-line in the absence of AWGN once we know the satellite channel characteristic according to the following steps:

1. Generation of S blocks of W symbols over which the SMF centroids are computed;
2. Computation of the error signal at the end of each block;
3. Pre-distorted constellation point update.

The latter task can be readily achieved through an iterative least mean square (LMS) type of algorithm illustrated by the following equations:

$$\rho_c^{(n)}(s) \exp\{j\theta_c^{(n)}(s)\} = \frac{1}{W} \sum_{k \in l^{(n)}, sW+1 \leq k \leq (s+1)W} z(k), \quad n = 1, \dots, M, \quad s = 1, \dots, S \quad (3)$$

$$e^{(n)}(s) = \rho_c^{(n)}(s) \exp\{j\theta_c^{(n)}(s)\} - c_{\text{TX}}^{(n)} \quad (4)$$

$$\rho_{c_{\text{TX}}}^{(n)}(s+1) = \rho_{c_{\text{TX}}}^{(n)}(s) - \gamma_\rho |e^{(n)}(s)| \quad (5)$$

$$\psi(s) = \begin{cases} \arg\{e^{(n)}(s)\} - 2\pi & \text{if } \arg\{e^{(n)}(s)\} > \pi \\ \arg\{e^{(n)}(s)\} + 2\pi & \text{elseif } \arg\{e^{(n)}(s)\} < -\pi \\ \arg\{e^{(n)}(s)\} & \text{if } -\pi \leq \arg\{e^{(n)}(s)\} \leq \pi \end{cases} \quad (6)$$

$$\theta_{c_{\text{TX}}}^{(n)}(s+1) = \theta_{c_{\text{TX}}}^{(n)}(s) - \gamma_\theta \psi(s) \quad (7)$$

where the index n refers to the constellation point, $l^{(n)}$ indicates the conditioning to the constellation point n , s refers to the iteration step of the algorithm, $z(k)$ represents the k th SMF output complex sample, $c_{\text{TX}}^{(n)}$ represents the constellation reference point, $\rho_c^{(n)}(s)$ and $\theta_c^{(n)}(s)$ are

the modulus and the phase of the SMF output complex n th centroid computed at step s , $\rho_{c_{TX}}^{(n)}(s)$ and $\theta_{c_{TX}}^{(n)}(s)$ are the modulus and the phase of the pre-distorted n th constellation point computed at step s , γ_ρ and γ_θ the adaptation steps for the modulus and the phase, respectively. Figure 12 provides a pictorial view of the pre-compensation algorithm. The static pre-compensation improvement on the 32APSK constellation is exemplified in Figures 13 and 14.

The static pre-distortion is able to correct for the constellation warping effects but it is not able to compensate the clustering phenomenon. For this purpose an extension of the static pre-compensation algorithm described in Reference [12] has been initially adopted and further improved. The dynamic pre-distortion algorithm takes into account the memory of the channel conditioning the pre-distorted modulator constellation not only to the current symbol transmitted but also to the $(L - 1)/2$ preceding and $(L - 1)/2$ following symbols (L symbols in total). This calls for an increased look-up table size of $T = M^L$ points. By exploiting the APSK constellation symmetry the amount of memory size can be reduced to $T = 3M^L/16$ for $M = 16$ and 32. The dynamic pre-distortion S memory coefficient calculation takes place offline by computer simulation of the satellite channel with the various modulation formats at the selected 'optimum' HPA operating point. The modulator will read in real-time the look-up table with an address determined by the current and the $(L - 1)/2$ precursors and post-cursors transmitted symbols.

The advantage provided by the dynamic pre-compensation on the reduction of the clustering effect can be assessed by observing the scatter diagram at the SMF sampler output shown in

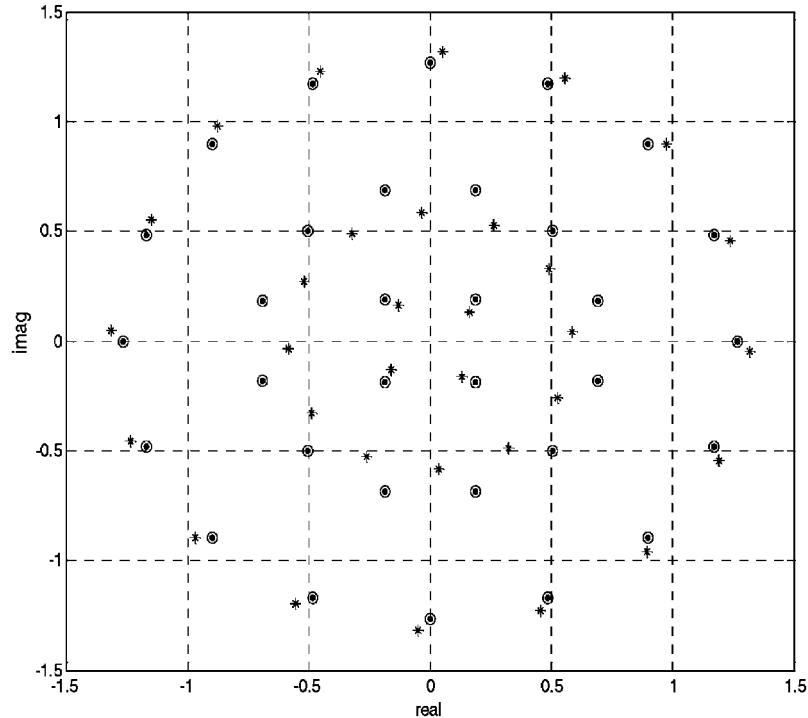


Figure 13. Static pre-distortion on 32APSK, with IBO = 4.6 dB, $W = 5000$ symbols, $S = 1500$ blocks: blue crosses: pre-distorted constellation; red circles: nominal constellation.

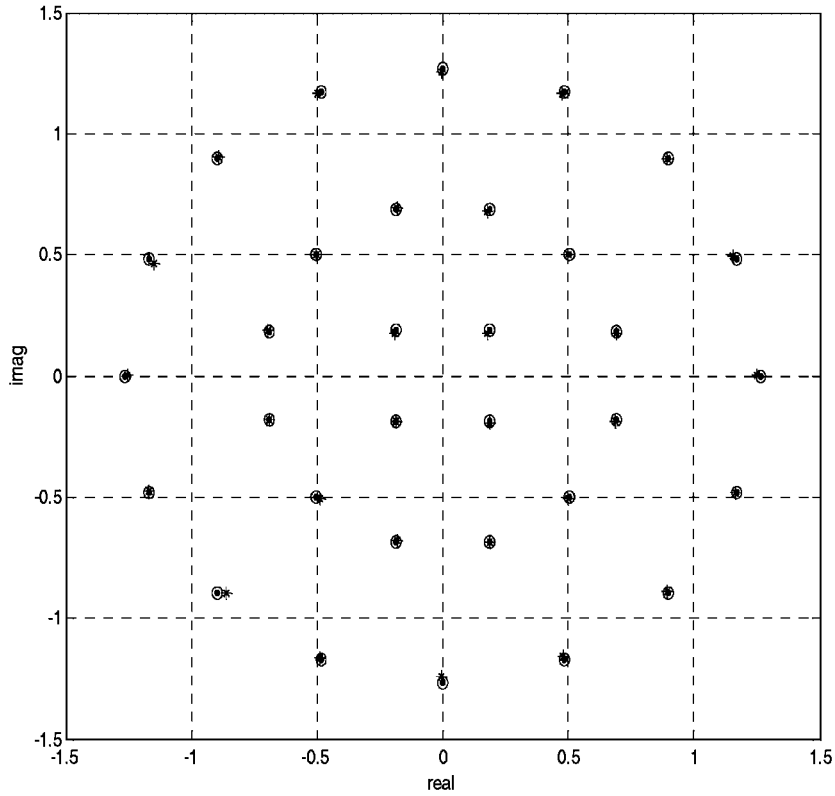


Figure 14. Static pre-distortion on 32APSK, with IBO = 4.6 dB, $W = 5000$ symbols, $S = 1500$ blocks: blue crosses: constellation centroids at the demodulator SMF; red circles: nominal constellation.

Figure 15(b) and 15(c). Looking at Figure 15(a) it appears that the clustering effect reduction is obtained at the expenses of an increased outer constellation points amplitude. This corresponds to a peak to average signal envelope ratio of 10 dB compared to 6.77 dB in the case of static pre-compensation. The dynamic pre-distortion induced peak-to-average increase has two main drawbacks: (a) the augmentation of the HPA output back-off (OBO) which negatively affects the overall system efficiency, (b) the possible impact on the HPA (TWTA) safe operation due to the higher peak-to-average ratio making the instantaneous signal power occasionally well beyond the saturation point.

Based on the previous considerations an improved dynamic pre-distortion approach has been devised. The quantity to minimize is in fact not the RMS of the centroids conditioned to a certain data pattern but rather the total link degradation D_{TOT} given by:

$$D_{TOT}(s)[\text{dB}] = \left[\frac{E_s}{N_0} \right]_{\text{req}}^{\text{NL}}(s)[\text{dB}] - \left[\frac{E_s}{N_0} \right]_{\text{req}}^{\text{AWGN}}(s)[\text{dB}] + \text{OBO}(s)[\text{dB}] \quad (8)$$

being $\left[E_s / N_0 \right]_{\text{req}}^{\text{NL}}$ and $\left[E_s / N_0 \right]_{\text{req}}^{\text{AWGN}}$ the average symbol energy over noise density required to achieve the target frame error rate (FER) in the non-linear and linear channel, respectively, and OBO the HPA output backoff. By using the Gaussian approximation for the ISI at the SMF

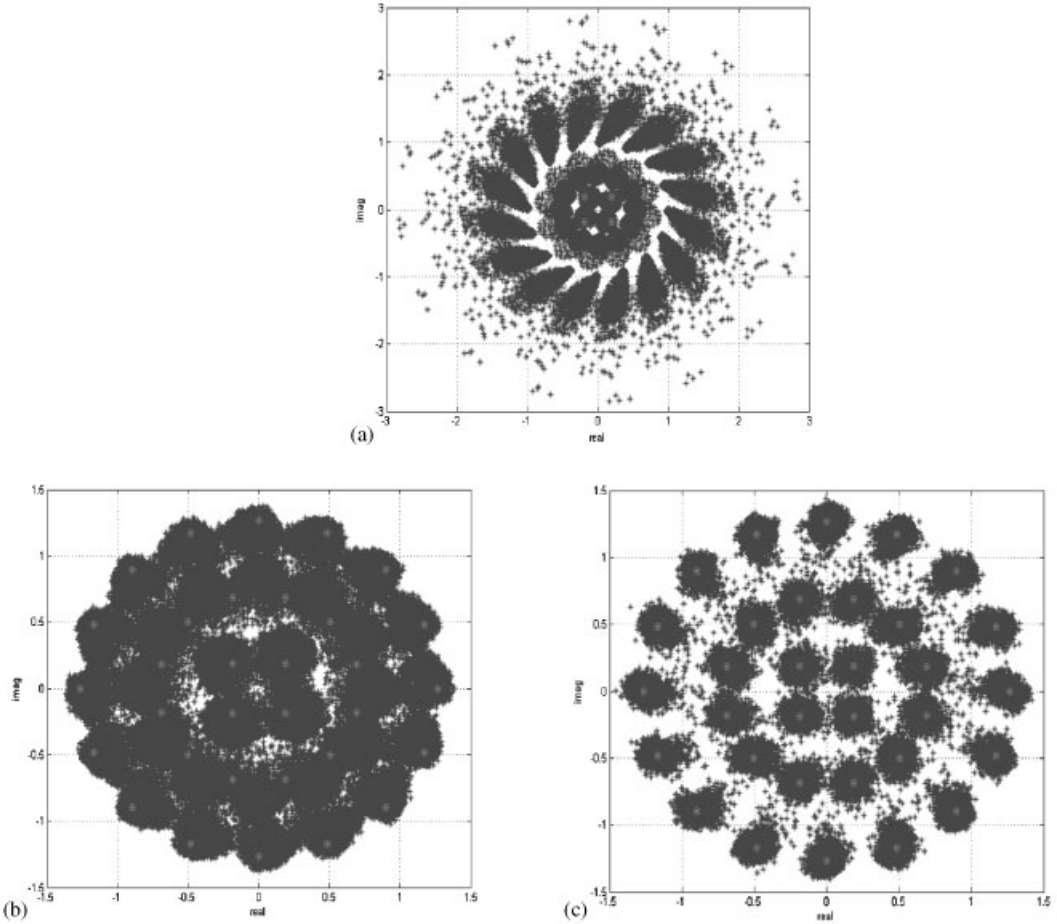


Figure 15. Dynamic pre-distortion on 32APSK, with IBO = 3.6 dB, $W = 5000$ symbols, $S = 85$ blocks, $L = 3$: (a) blue crosses: pre-distorted constellation; red circles: nominal constellation. (b) Blue crosses: constellation centroids at the demodulator SMF without pre-compensation; red circles: nominal constellation. (c) Blue crosses: constellation centroids at the demodulator SMF with dynamic pre-compensation; red circles: nominal constellation.

sampler output one can write:

$$\left[\frac{E_s}{N_0} \right]_{\text{req}}^{\text{NL}}(s) = \left[\frac{E_s}{N_0} \right]_{\text{req}}^{\text{AWGN}}(s) \left[1 + \frac{\sigma_{\text{ISI}}^2(s)}{N_0} \right] \quad (9)$$

where $\sigma_{\text{ISI}}^2(s)$ represents the ISI power at the output of the SMF averaged over the constellation points at step s :

$$\sigma_{\text{ISI}}^2(s) = \frac{1}{M} \sum_{n=1}^M \sum_{k \in l^{(n)}, sW+1 \leq k \leq (s+1)W} |z(k) - c^{(n)}|^2 \quad (10)$$

and N_0 represents the thermal noise power spectral density. Then, by replacing (9) in (8) we get:

$$D_{\text{TOT}}(s) = \left[1 + \frac{\sigma_{\text{ISI}}^2(s)}{N_0} \right] \text{OBO}(s) \quad (11)$$

Equation (11) is valid in the case of absence of intra-system co-channel and adjacent channel interferences. These two quantities, in fact, depend on the signal energy so that an increase of the OBO does not affect the signal-to-interference ratio. It is easy to show that, called I_0^{SAT} the total power of the intra-system interference samples at the SMF output with OBO = 0 dB, Equation (11) can be generalized as follows:

$$D_{\text{TOT}}(s) = \left[1 + \frac{\sigma_{\text{ISI}}^2(s) + I_0^{\text{SAT}}/\text{OBO}(s)}{N_0} \right] \text{OBO}(s) \quad (12)$$

Since I_0^{SAT} is system-dependent, in the following we will assume a situation where intra-system interference is negligible, so that its contribution does not affect the pre-distortion optimization results.

The dynamic pre-compensation is now performed as before computing every block of W symbols also the σ_{ISI}^2 and OBO and computing (11) at each step. The dynamic pre-compensation is now stopped when the minimum of D_{TOT} is achieved. This approach ensures the best trade-off between ISI minimization and the OBO penalty due to the increased peak-to-average ratio caused by dynamic pre-compensation. To speed-up process convergence and to avoid bias in the σ_{ISI}^2 estimate, the static pre-compensation is first applied then the dynamic pre-compensation is started. This approach allows beginning the dynamic pre-compensation with the SMF centroids very close to the nominal constellation points. An example of the D_{TOT} -based optimized dynamic pre-compensation is illustrated in Figure 16. In this figure the D_{TOT} and OBO evolution versus the iteration number s is plotted for the case of 8PSK. It appears that after the minimum of D_{TOT} occurring around $s = 30$ blocks, after this value the total loss is growing following the OBO growth due to the transmit constellation outer points expansion. In the following simulation results, when not stated otherwise, we stopped the dynamic pre-distortion adaptive algorithm at the optimum instant.

3.2. Clock recovery

Symbol clock recovery can be performed first using the well-known Gardner's algorithm [13]. This algorithm is non-data aided (NDA) and thus can be run without any frame synchronization in place. The performance of this algorithm is quite insensitive to the modulation format at least over the range of E_s/N_0 of interest as well as to a carrier frequency error up to 0.1–0.2 times the symbol rate. That means that for 25 Mbaud symbol rates, the timing recovery can work with a carrier frequency error up to 5 MHz. For lower symbol rates (down to 10 Mbaud) a possible technique is to use two timing recovery algorithms working in parallel. The first with a signal pre-rotated in frequency by $+\frac{1}{4}$ of the symbol rate (F_s) and the second with $-\frac{1}{4}$ of F_s . Then, after pre-determined time left for the transient, the algorithm that has converged can be selected. The jitter RMS of the algorithm depends on the signal roll-off factor. In particular, it worsens as the roll-off decreases. For the DVB-S2 range of roll-offs and E_s/N_0 , a normalized (to the symbol rate) loop bandwidth of 5×10^{-5} seems to be required for negligible impact to the receiver performance. With this loop bandwidth and using a second order loop, a clock frequency error of 10 ppm can be tracked with no residual error bias. Also, the overall acquisition transient of the timing recovery unit would be around 10^5 symbols, which corresponds to 5 ms at $F_s = 25 \times 10^6$.

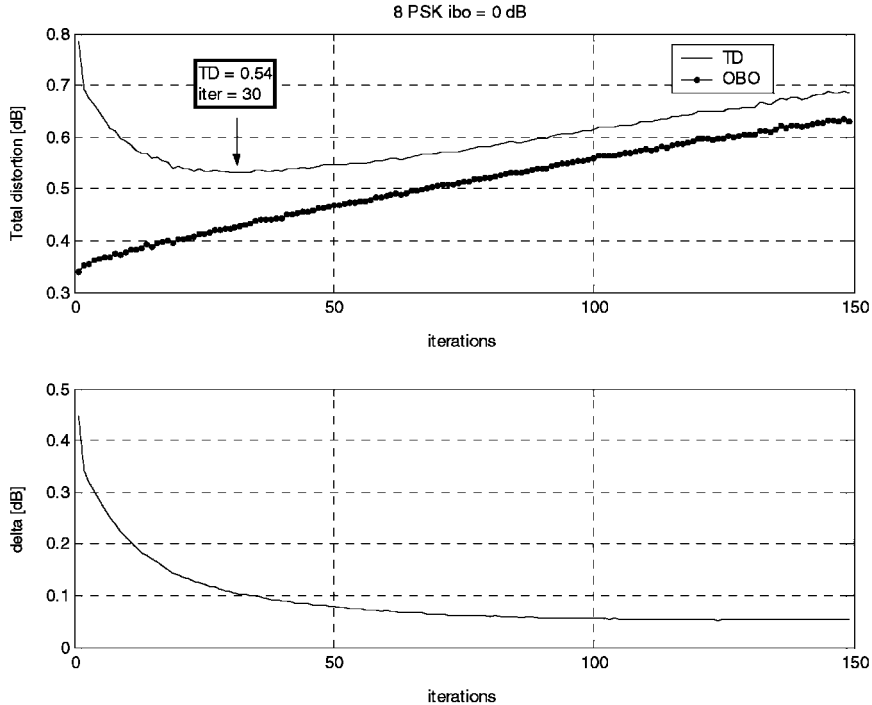


Figure 16. Total degradation D_{TOT} (TD in the plot) and OBO evolution versus time with dynamic pre-distortion on 8PSK, with IBO = 0 dB, $W = 50\,000$ symbols.

3.3. Physical layer frame synchronization

After the receiver symbol timing has reached steady state the next step to be performed is frame synchronization by searching for the physical layer header. This can be performed even in the presence of a strong carrier frequency error through differential detection. Reference [14] shows that the mean acquisition time is around 20 ms for 25 Mbaud transmissions at $E_s/N_0 = -2$ dB and less than 4 ms at $E_s/N_0 = 0.7$ dB (these numbers are approximately the operating E_s/N_0 values of OPSK $r = 1/4$ and OPSK $r = 1/2$, respectively). At 99% probability the acquisition time for frame synchronization is around 130 ms at $E_s/N_0 = -2$ dB and 10 ms at $E_s/N_0 = 0.7$ dB.[†] In case of the unicast profile exploiting ACM, until the carrier frequency and phase synchronization estimators are not in steady-state condition the physical layer frame configuration field (MODCOD) [1] cannot be decoded. Hence pilot locations for successive frames shall be determined based on PLHEADER synchronization verification at the four possible locations (one per modulation format). Once carrier phase synchronization has been established, then the position of the pilot symbols is also known (by decoding the MODCOD fields of the PLHEADERS of each physical layer frame [XFECFRAME]).

3.4. Carrier frequency recovery

As the carrier phase recovery unit (the linear interpolator in particular) tolerates residual normalized carrier frequency offsets up to 3.5×10^{-4} , the task of this unit is to bring the

[†]Those acquisition times can be largely improved by using more complex frame detection schemes.

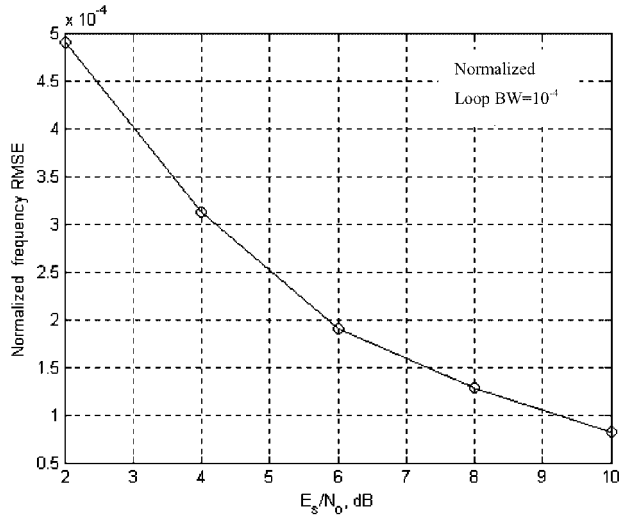


Figure 17. Tracking performance of the coarse carrier frequency synchronizer.

precision of the recovered carrier frequency down to that max value. If we assume that the frequency error is Gaussian distributed,^{||} that means that the normalized standard deviation of the frequency jitter has to be lower than 5.3×10^{-5} , for a probability that the max be exceeded lower than 10^{-11} . The initial max frequency uncertainty is around ± 5 MHz, which represents 20% of the symbol rate at 25 Mbaud. For this large frequency error, a simple PA carrier recovery technique exists which can perform a first coarse frequency recovery [7]. The algorithm can be implemented in a feedback structure where a second-order loop filter drives an NCO and is fed by a frequency error detector (FED) that implements the following equation:

$$e(k) = \text{Im} \{ z^{(p)}(k) c^{(p)*}(k) z^{(p)*}(k-2) c^{(p)}(k-2) \} \quad (13)$$

where $z^{(p)}(k)$ are the signal samples at the matched filter output corresponding to the pilot symbols $c^{(p)}(k)$. The loop is active only during the pilot symbols and is frozen (i.e. the value of the frequency estimate is kept constant) during the data symbols.

Figure 17 shows the tracking performance of the coarse frequency synchronizer in terms of RMS of the estimation error for a loop bandwidth normalized to the symbol rate of 10^{-4} . The simulation results shown in the figure refer to a continuous operation mode (i.e. continuous stream of pilots with no data in between) but as it turns out, the loop freezing does not impact the jitter performance significantly. When working with pilots and data, the effective loop bandwidth (for the purpose of acquisition time) reduces by a factor of $\varsigma = (L_p - 2)/L_s = 0.023$ as far as the acquisition time is concerned.^{**} See for example Figure 18 where the frequency acquisition is shown for SNR = -2 dB and a normalized loop bandwidth of 10^{-4} .

^{||}The assumption has been validated with good approximation in the case of interest by extensive Monte Carlo simulations.

^{**}Note that the -2 at the numerator is due to the fact that the raw frequency estimator needs samples at a distance of 2 symbols.

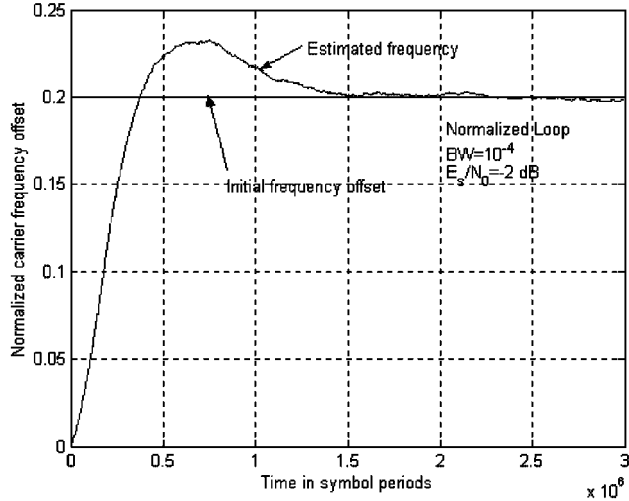


Figure 18. Coarse carrier frequency acquisition transient.

Extensive simulations have shown that, for the worst case and with the required range of E_s/N_0 , this synchronizer is able to bring the max value of the frequency error down to 100 kHz (which normalized to the symbol rate of 25 Mbaud corresponds to 4×10^{-3}) in about 100 ms by using a normalized loop bandwidth of 10^{-4} . Note that this coarse frequency acquisition in theory needs to be run only at system initialization when the max carrier frequency error can be as large as 5 MHz. For channel zapping in broadcast mode, as a result of a channel tuning the specified maximum short-term normalized carrier frequency uncertainty is less than ± 100 kHz. Hence, in principle once the nominal acquisition time of the coarse carrier recovery unit is passed, this unit could be frozen and its NCO kept running with the last frequency estimate. However, due to very slow carrier frequency drifts, it is required to let this coarse frequency acquisition unit running also after initial acquisition but with a reduced loop bandwidth, say 10 times less.

Fine frequency estimation completes the carrier frequency acquisition process. This is accomplished by a pilot-based feedforward algorithm derived from the L&R technique [15] and whose block diagram is depicted in Figure 19.

The deviation from the known L&R algorithm is that here the mean N point autocorrelation function $\sum_{m=1}^N R(m)$ is also averaged over L consecutive pilot fields before computing the argument function. The expression of the frequency estimate thus reads:

$$\hat{v}T = \frac{1}{\pi(N+1)} \arg \left\{ \sum_{l=1}^L \sum_{m=1}^N R_l(m) \right\} \quad (14)$$

where $R_l(m)$, for $m = 1, \dots, N$, are the N points autocorrelation vector computed over the l th pilot symbol fields (36 symbols according to the standard [8]) i.e.

$$R_l(m) = \frac{1}{L_p - m} \sum_{k=m}^{L_p-1} z^{(p)}(k + lL_s) c^{(p)*}(k + lL_s) z^{(p)*}(k - m + lL_s) c^{(p)}(k - m + lL_s) \quad (15)$$

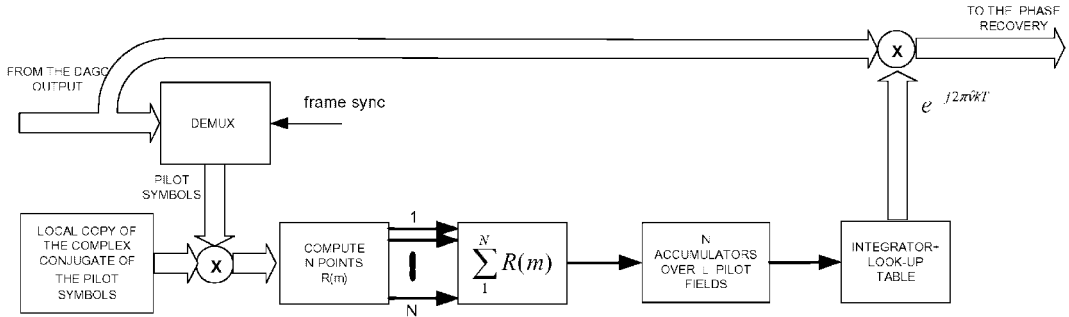


Figure 19. Block diagram of the fine frequency estimator.

and $L_p = 36$, $L_s = 1476$ (see Section 3). By simulation it has been found that with $L = 1000$ and $N = 18$, the RMS of the residual normalized frequency error RMS is 6×10^{-5} at $E_s/N_0 = -2$ dB, 5.2×10^{-5} at $E_s/N_0 = 1$ dB, 2.72×10^{-5} at $E_s/N_0 = 6.6$ dB and 1.82×10^{-5} at $E_s/N_0 = 10$ dB. Therefore, with this configuration it is guaranteed that the RMS is below the target of 5.3×10^{-5} for SNRs down to about 1 dB. The acquisition time for this algorithm is 1000 pilot fields, that is about 60 ms at 25 Mbaud. No outliers have been recorded over long simulations at SNR as low as -2 dB and with frequency error of 100 kHz. However, in this case the parameter L has to be increased to about 2500 in order to get the required jitter RMS.

3.5. Automatic gain control

The automatic gain control (AGC) represents an important demodulator sub-system. In fact, the decoder needs accurate soft information about the received symbol distance from the reference constellation points. The soft information accuracy is critically dependent on the channel estimation, i.e. symbol, clock timing, carrier phase and signal amplitude normalization. The AGC deals with the latter estimation. In DVB-S2 interactive profile the task of the AGC is complicated by the presence of a frame-by-frame variant physical layer. In Reference [10] a complex decision-directed vector tracker (DD-VT) and a non-coherent non-decision-directed (NDD) amplitude AGC schemes for 16QAM were derived and their performance analysed. The DD vector tracker estimates both the amplitude and the phase of the QAM signal and results to be practically unbiased if the decision errors are below 10^{-2} . The non-coherent NDD scheme is instead unacceptably biased for $E_s/N_0 < 10$ dB. As our AGC has to operate over a wide range of SNR ($-2.5 < E_s/N_0 < 16$ dB) a robust yet simple scheme has to be selected. It is proposed to use the pilot symbols exploited for the carrier phase estimation also for AGC thus adopting the data-aided version of the vector-tracker AGC (DA-VT AGC). This means that the AGC will only be activated in the presence of the pilot symbols and amplitude normalization frozen in between consecutive pilots. As pilot symbols are QPSK scrambled at physical layer, their constellation amplitude may in general be characterized by a different energy than the frame PL data due to the satellite HPA distortion effects. This unwanted effect can be easily removed applying the (static) pre-distortion technique to the pilot symbols too and by ensuring that the

pilot symbols average energy at the HPA output is the same as the PL symbols one.^{††} Furthermore, although a DA-VT-AGC has been selected, to avoid unwanted interactions with the carrier phase estimator sub-system described in next section, we only use the real amplitude of the complex AGC estimate to normalize the signal power. Following [10], the DA-VT-AGC equations are

$$s(k) = A_k z(k), \quad A_k = |\alpha_k| \quad (16)$$

$$\alpha_{k+1} = \begin{cases} \alpha_k - \gamma_{\text{AGC}} [\alpha_k z^p(k) - c^p(k)] c^p(k)^* & \text{for } k \in \text{pilot symbols} \\ \alpha_k & \text{otherwise} \end{cases} \quad (17)$$

being $z(k)$ the k th SMF complex sample, A_k the k th real AGC constant, $s(k)$ the k th complex signal sample after the AGC, α_k the k th DA-VT AGC complex coefficient, γ_{AGC} the AGC adaptation step, $c^p(k)$ the k th pilot symbol. A non-PA AGC will need to remove the PL data by using some reliable symbol estimates to get an unbiased estimate that complicate the demodulator processing. Also in this case the modulator pre-distortion shall ensure that the received constellation centroids are characterized by the same energy for all possible physical layer constellation configurations even when operating the satellite HPA close to saturation.

3.6. Carrier phase recovery

The carrier phase recovery unit has to cope with a residual carrier frequency error from the carrier frequency recovery unit as well as a strong phase noise. To this end, a very simple PA technique exists which provides satisfactory results at least for low order modulations (QPSK and 8PSK), while for 16 and 32APSK some extra data-tracking algorithm is needed. We start with describing the PA technique, which is all is needed for QPSK and 8PSK modulations.

3.6.1. PA linear interpolation. The PA interpolation techniques consists in deriving the phase trajectory over the data symbols by just linear interpolation of estimates performed over two consecutive pilot fields. As the symbols transmitted over the pilots are known, it is clear that the best estimator that can be used there is the maximum likelihood (ML) estimator [7, Chapter 5]. Also, as the L_p is short a feedforward (FF) approach is also suggested in order to speed up the required estimation process.

The block diagram of the FF ML estimator is represented in Figure 20 where the variables with superscript ‘p’ indicate that they refer to the pilot symbols.

The phase estimate is carried out by collecting the L_p matched filter output samples $z^p(k)$ at baud rate corresponding to the pilot fields, and performing the following algebraic operations:

$$\hat{\theta}^{(p)} = \arg \left\{ \sum_{k=0}^{L_p-1} [c^{(p)}(k)]^* z^{(p)}(k) \right\} \quad (18)$$

It is clear from (18) that just one estimate is provided every pilot field, so if the carrier phase is actually time variant due to a phase noise or an uncompensated carrier frequency error, the

^{††}As this tuning is performed off-line with the nominal HPA characteristic, some residual mismatch between the pilot and the payload symbols may result. If necessary, this effect may be compensated by a fine NDA DAGC carried out over, the payload symbols.

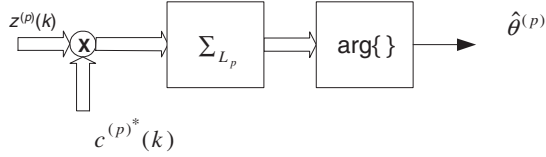


Figure 20. FF ML phase estimator.

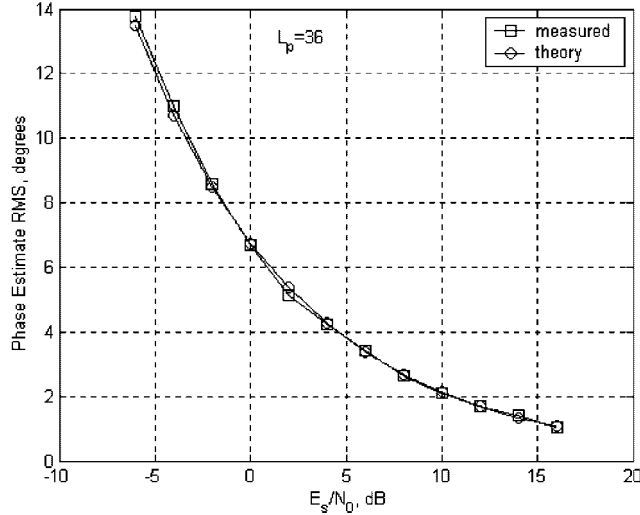


Figure 21. Phase estimate RMS of the FF ML synchronizer (theory and simulation results).

estimate provided will be an average of the phase evolution during the pilot field. However, if L_p is small and the phase process relatively slow, the time variation property of the carrier phase can be neglected. Under this hypothesis and with relatively high signal-to-noise ratio, it can be shown (see Reference [7, Chapter 5]) that (18) can be re-written as

$$\hat{\theta}^{(p)} \cong \theta + N_I \quad (19)$$

with N_I being the zero-mean Gaussian noise contribution to the phase estimate, with variance:

$$\sigma_{N_I}^2 \cong \sigma_{\hat{\theta}^{(p)}}^2 = \frac{1}{2L_p E_s / N_0} \quad (20)$$

which is independent from the modulation used in the pilot fields.

Also it is worth noting that under the assumption of ideal matched filtering (the noise samples at symbol rate at its output are white), the process consisting of the sequence of noise samples N_I relative to different pilot fields, is white, as no correlation exists between the noise in different pilots.

As we pointed out, Equation (20) is valid under the assumption of high SNR so that Equation (19) holds. For very low SNR a departure of the phase estimate variance from (20) is expected, as shown in Figure 21 where simulation results are compared to (20) (even though for $L_p = 36$, the differences are very small down to -6 dB).

The linear interpolation technique makes use of the phase estimates performed over consecutive pilot fields to derive the vector of phase estimates over the data portion of the slot. In these cases, as the FF ML estimator (18) provides a phase estimate in the interval $[-\pi, \pi]$ while the true carrier phase may grow beyond this range over a time slot period, in order to be able to consistently use the pilot-based estimates, an unwrapping technique has to be applied to these latter. This can follow the approach outlined in Reference [16] and depicted in Figure 22.

If the index ' l ' counts the number of pilot-based estimates, the final unwrapped pilot estimates $\hat{\theta}_{(f)}^{(p)}(l)$ are computed from $\hat{\theta}^{(p)}(l)$ as

$$\hat{\theta}_{(f)}^{(p)}(l) = \hat{\theta}_{(f)}^{(p)}(l-1) + \alpha \text{SAW}[\hat{\theta}^{(p)}(l) - \hat{\theta}_{(f)}^{(p)}(l-1)] \quad (21)$$

where $\text{SAW}[\Phi] \equiv [\Phi]_{-\pi}^{+\pi}$ is a saw tooth non-linearity that reduces Φ to the interval $[-\pi, \pi]$ and α is a parameter in the range $0 < \alpha \leq 1$, which in the following we will assume equal to 1.

It is easy to verify that Equation (21) provides a good final unwrapped pilot phase estimate, provided the difference between the carrier phase in the current pilot field and the final estimate $\hat{\theta}_{(f)}^{(p)}(l-1)$ on the previous slot is less than π . If that condition is not met, we can think of the feedback algorithm of Figure 22 as in a cycle slip. This can be the case, for example, when as a result of a residual carrier frequency offset Δv , the carrier phase grows linearly over two consecutive pilot fields of more than π , i.e.

$$2\pi\Delta v L_s T \geq \pi \Rightarrow \Delta v T \geq \frac{1}{2L_s} \quad (22)$$

where L_0 is the distance between pilot fields in number of symbols, i.e. 1476.

Equation (22) poses a limit on the maximum value of the residual normalized frequency error that the unwrapping algorithm can cope with without cycle slips. The longer the distance between pilot symbols, the smaller the max sustainable frequency offset. For $L_s = 1476$ the max sustainable normalized carrier frequency errors turns out to be 3.4×10^{-4} .

Note that (22) takes into account the requirement due only to the carrier frequency offset; when thermal noise is also considered, the cycle slip rate may increase. In particular, under the assumption of high SNR, Equation (19) indicates that the phase estimates out of the FF ML estimator are Gaussian and independent so that one could compute the probability that a cycle slip occur as

$$P_{cs} = \Pr\{|\theta^{(p)}(l) - \theta^{(p)}(l-1)| > \pi\} = 2 \int_{\pi}^{\infty} \frac{1}{\sqrt{4\pi\sigma_{N_l}^2}} e^{-x^2/4\sigma_{N_l}^2} dx \quad (23)$$

Figure 23 shows the cycle slip probability P_{cs} as function of E_s/N_0 for $L_p = 36$, as in (23). If one wants to design the system with baud rate F_s in order to have less than 1 cycle slip event per hour of transmission, the probability of cycle slip has to be set to less than $L_s/(3600 F_s)$, which corresponds to the inverse of the number of pilot field-based phase estimates per hour. For example, with $F_s = 25 \times 10^6$ and $L_s = 1476$, the requirement on P_{cs} results to be 16.4×10^{-9} .

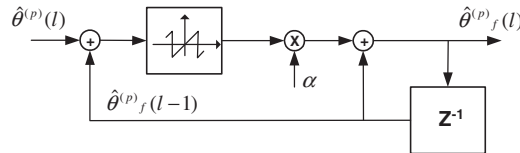


Figure 22. The unwrapping algorithm.

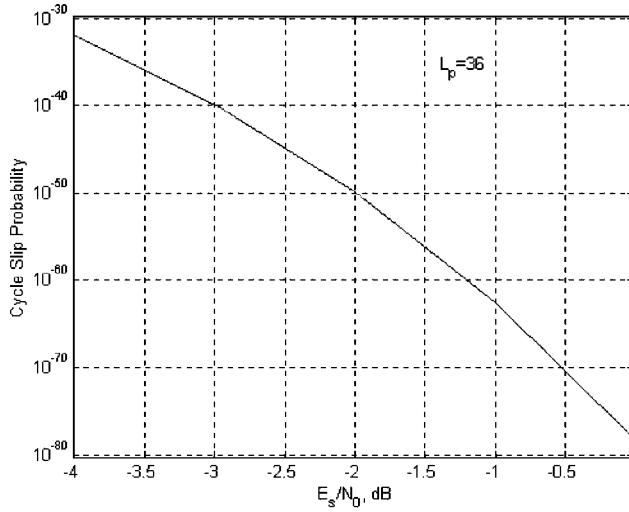


Figure 23. Cycle slip probability of the phase unwrapping algorithm.

From Figure 23 it turns out that requirement is largely met for any value of the operating E_s/N_0 . The cycle slip rate also increases due to the presence of phase noise and carrier frequency offsets. In practice only long simulations can assess the rate of cycle slips. This is reported in Section 4. An additional point to make about the cycle slip properties of the unwrapping technique of Figure 22 is that phase cycle slips occur in multiple of 2π as it is now shown. To this end let us consider Equation (21) that we now re-write by taking into account that (i) the saw tooth function introduces a phase jump of a multiple of 2π ($n2\pi$) and (ii) the phase estimate at the output of the FF ML estimator differs from the true one by a multiple k of 2π (besides the estimation error):

$$\begin{aligned}\hat{\theta}_f^{(p)}(l) &= \hat{\theta}^{(p)}(l-1) + \hat{\theta}^{(p)}(l) - \hat{\theta}_f^{(p)}(l-1) \pm n2\pi \\ &= \hat{\theta}^{(p)}(l) \pm n2\pi = \theta^{(p)}(l) \pm k2\pi \pm n2\pi\end{aligned}\quad (24)$$

Then, from (24) one can see that the final un-wrapped estimate always differ from the true one by a multiple of 2π , which means that at least over the pilot fields the phase estimates are always correct. The problem results when interpolating two consecutive phase estimates when a cycle slip has occurred as that would lead to a bad interpolation over the slots comprised between the two pilots.

Once the unwrapped FF-ML phase estimates are performed, linear interpolation between consecutive pilot-based estimates can be carried out. This is pictorially described in Figure 24. In order to compute the interpolants for the current (\bar{l} th) pilot repetition period, the interpolator makes use of only the FF ML estimates of the pilot fields of the l th period and the one of the next period ($(\bar{l}+1)$ th) according to the following equation:

$$\hat{\theta}(k_s) = \hat{\theta}(\bar{l} \cdot L_s) + [\hat{\theta}((l+1) \cdot L_s) - \hat{\theta}(\bar{l} \cdot L_s)] \left(\frac{k_s}{L_s} \right) \quad (25)$$

where $k_s = 1, 2, \dots, L_s - 1$, is the symbol index within the pilot repetition period.

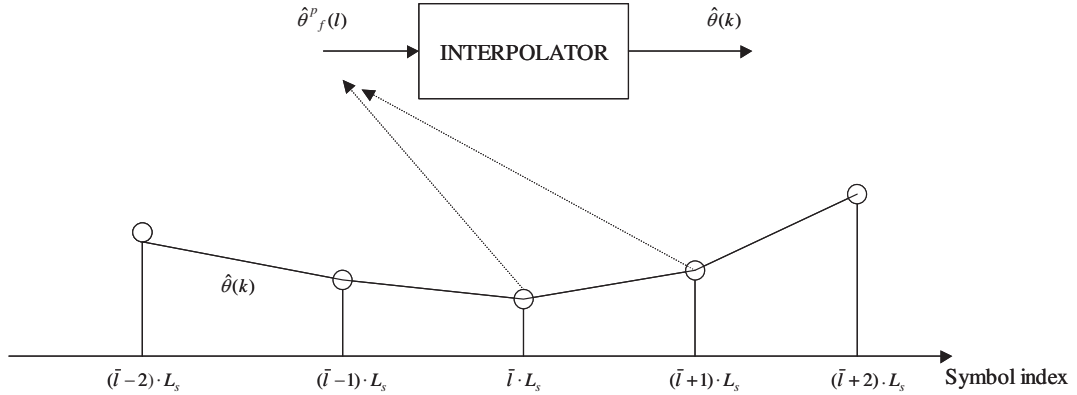


Figure 24. Linear interpolation technique.

Some extra care should be paid when computing the pilot-based phase estimate on the pilot field where the feed-forward fine frequency estimator performs its correction too. In fact, as result of the update of the carrier frequency, a jump in the carrier phase may result thus affecting the linear interpolation algorithm. In order to cope with this effect, it is recommended to perform two phase estimates over the pilot field where the carrier frequency is also updated: the first, to be used to interpolate with the previous pilot-based phase estimate, with the old carrier frequency, the second, to be used to interpolate with the next pilot-based phase estimate, with the updated carrier frequency. With the recommended acquisition parameters this would take place once every 1000 pilots.

The performance of this very simple algorithm has been assessed in terms of phase error jitter RMS in the presence of phase noise and with a normalized carrier frequency error of 10^{-4} , for 25 Mbaud transmission rate. The results are shown in Figure 25.

As expected the error RMS decreases with the E_s/N_0 value, but it tends to reach a floor at about 3 degrees for large values of E_s/N_0 . This is due to the reason that even in absence of noise, the phase estimator is not able to track the phase noise trajectory within the data portion of the pilot repetition period. A more efficient technique would be to use a Wiener filter interpolation technique over the data symbols, even though the expected performance improvements do not justify the added complexity. Therefore, it is expected that for high-order and more phase jitter sensitive modulations like 16APSK and 32APSK a data symbol phase tracking algorithm needs to be used to limit the performance degradation. This is addressed by the Fine Phase recovery unit which is described in the next sub-section.

3.6.2. Fine phase recovery for high-order modulations. The best NDA algorithms that we have found in literature for 16 and 32APSK are described in Reference [11]. Here we summarize their structures.

They consist of Q th power close-loop NDA phase synchronizers whose block diagram is depicted in Figure 26. The corresponding phase error detector algorithm has the following form:

$$q(k) = [z(k)]^Q e^{j\beta} \quad (26)$$

$$e_\phi(k) = \text{Im}\{q(k)(\text{sign}[\text{Re}\{q(k)\}] - j \text{sign}[\text{Re}\{q(k)\}])\} \quad (27)$$

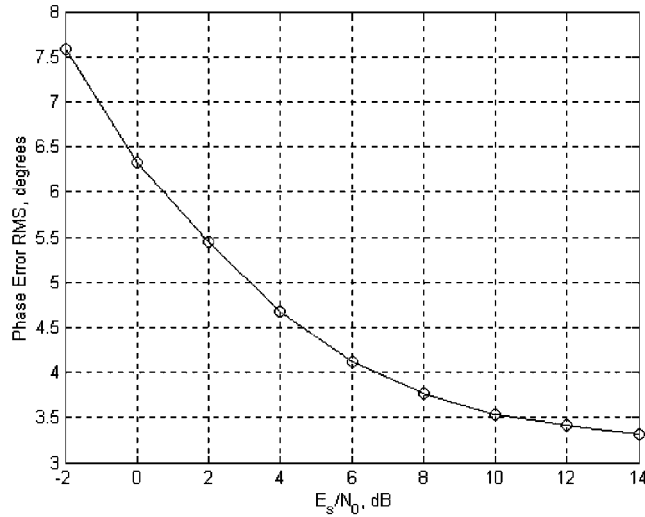


Figure 25. Phase error RMS of the PA-LI technique as function of E_s/N_0 .

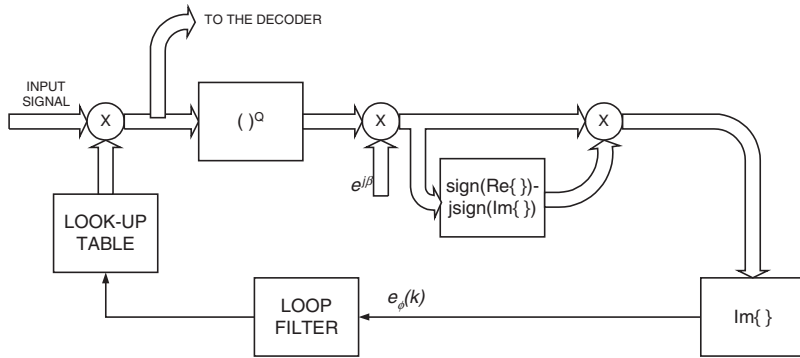


Figure 26. Fine phase recovery unit.

where β is a fixed phase rotation of 0 radians for 16APSK and $\pi/4$ for 32APSK, while Q is 3 for 16APSK and 4 for 32APSK.

Raising a $4+12$ APSK constellation to the 3rd power (in the complex domain), the original $4+12$ APSK constellation approximately transforms into a QPSK one [11]. It is easy to see that the external ring points fall into a QPSK ring, while the internal points collapse towards the origin. Hence, a four-quadrant closed loop phase estimator can be efficiently applied to the cubic non-linearity output. Same considerations apply when raising the 32APSK constellation to the 4th, although now a $\pi/4$ phase shift is required to have the same decision zones as before. Note that most remarkable features of this algorithm are its simplicity and that it is relatively insensitive to amplitude errors due to the quadrant slicing operation involved. This would not apply to a full hard decision-directed scheme implementing the 16 and 32APSK constellation hard decision rules.

Please refer to Reference [11] for a comprehensive analysis of the performance of this algorithm. The fine phase recovery unit works at the output of the PA-LI unit and its memory

(loop filter) is reset once every pilot field. This greatly helps in reducing the probability of cycle slips under reasonable values. The digital AGC block is placed just before the fine carrier recovery unit in order to guarantee a precise setting of the loop bandwidth, as this is important in order to optimize the loop performance and minimize the system loss.

4. PERFORMANCE RESULTS

In this section we show end to end performance results for QPSK, 8PSK, 16 ASQSK and 32APSK modulations assuming linear channel (Section 4.1) and non-linear channel with pre-compensation (Section 4.2), and with the proposed carrier synchronization algorithms in the presence or not of phase noise and carrier frequency error. In these simulations timing is considered ideal, as the inclusion of the timing recovery algorithm within the end-to-end simulation program would have significantly slowed down the simulations. However, its impact into performance is minimal for all the modulation schemes, as long as the design guidelines outlined in Section 3.2 are met.

Simulations have been running with a roll-off of 0.3. Even though this value is not strictly part of the standard we can say that (i) it represents a sort of mean value among the ones in the standard (0.2, 0.25 and 0.35), (ii) the impact of the roll-off into the performance of the carrier synchronization scheme is negligible. The assumed baud rate is 25 Mbaud, which represents a realistic value for the minimum symbol rate value for the forward link of a broadband satellite transponder. Lower symbol rates are expected to have slightly worse performance, as the phase noise impact to the performance is higher. However, lower Baud rates are associated to professional applications for which better RF front-ends are typically used. The assumed initial carrier frequency error is 5 MHz and both the coarse and fine frequency recovery is active. The linear interpolation technique is supposed to be the only active phase recovery scheme for QPSK and 8PSK modulations, while for 16APSK and 32APSK the fine phase DPLL is supposed to be active too. The simulation program contains a model for the transmitter and received SRRCFs. These filters have ideally an infinite length. In our simulations we have limited their duration to 20 symbol intervals without any particular optimization. That has proven to lead to an overall performance degradation of about 0.1 dB, with respect to the ideal case. All the simulation results with imperfect synchronization and on the non-linear channel have been compared to the AWGN performance with these realistic filters.

Performance losses are due to both E_s/N_0 penalties due to synchronization jitter and channel non-linear distortions, plus efficiency loss due to the presence of the pilot symbols. In order to combine the two, the total loss with respect to the ideal AWGN case will be computed in the efficiency versus E_s/N_0 graph by calculating the ratio between the distance of the operating point to the modulation-constraint capacity bound for the AWGN case with no pilots and for the real system with pilots and imperfect synchronization/channel distortions.

4.1. Impact of imperfect synchronization

The overall impact of imperfect carrier synchronization has been assessed by means of long simulations. As the simulation program models many sub-systems working in the demodulator and the decoder at the same time, it does not allow to achieve very low BER value estimates in a reasonable short time. Thus we had to stop our analysis at a BER value around 10^{-5} – 10^{-6} .

although a number of checks have been done to ensure the correct synchronizer operations at lower BER. When the fine phase recovery PLL is exploited its loop bandwidth at the SNR corresponding to a $\text{BER} = 10^{-5}$ has been optimized in the presence of phase noise to minimize the phase error jitter variance. Optimum normalized loop bandwidths resulted to be $B_L T_s = 3.5 \times 10^{-4}$ for 16APSK operating at $E_s/N_0 = 10.5 \text{ dB}$ and $B_L T_s = 5.6 \times 10^{-4}$ for 32APSK operating at $E_s/N_0 = 14 \text{ dB}$.

Figures 27 and 28 show the BER curves for QPSK/8PSK and 16APSK/32APSK, respectively. Pilot overhead is not taken into account in these plots. As seen, the $\Delta E_s/N_0$ degradation is very small for QPSK ($r = \frac{1}{2}$) and 8PSK ($r = \frac{2}{3}$) (about 0.1 dB for QPSK ($r = \frac{1}{2}$) and 0.25 dB for 8PSK ($r = \frac{2}{3}$)) even though only the linear interpolator is used as carrier recovery circuit, thus confirming that no data tracking phase recovery system is needed for these modulations. For 16APSK the loss is about 0.35 dB at $\text{BER} = 10^{-7}$ with the fine phase DPLL running. An additional loss of 0.15 dB is paid if the fine phase DPLL is turned off. 32APSK shows a loss of about 1.05 dB at $\text{BER} = 10^{-7}$ with an additional loss of 0.2 dB if the DPLL is deactivated. To note that for 32APSK a better phase noise mask should be adopted considering the more professional type of applications to be supported. If the phase noise mask PSD is scaled down by 3 dB, the 32APSK synchronizer loss reduces to only 0.3 dB when the PLL for fine carrier estimation is activated.

However, it is important to note that, at least over the time spans of the simulation runs, no cycle slip event have been recorded, thus confirming the robustness of the proposed design.

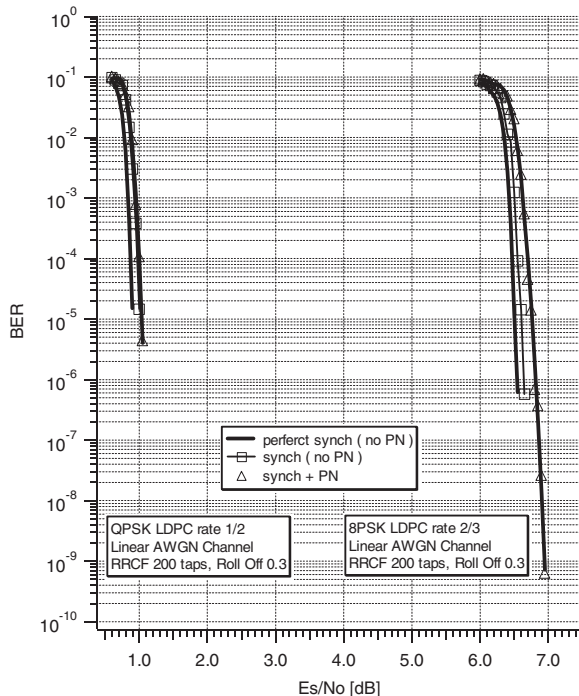


Figure 27. BER curves of QPSK $r = \frac{1}{2}$ and 8PSK $r = \frac{2}{3}$ over an ideal linear channel and with the proposed carrier synchronization scheme in case of no phase noise or phase noise presence.

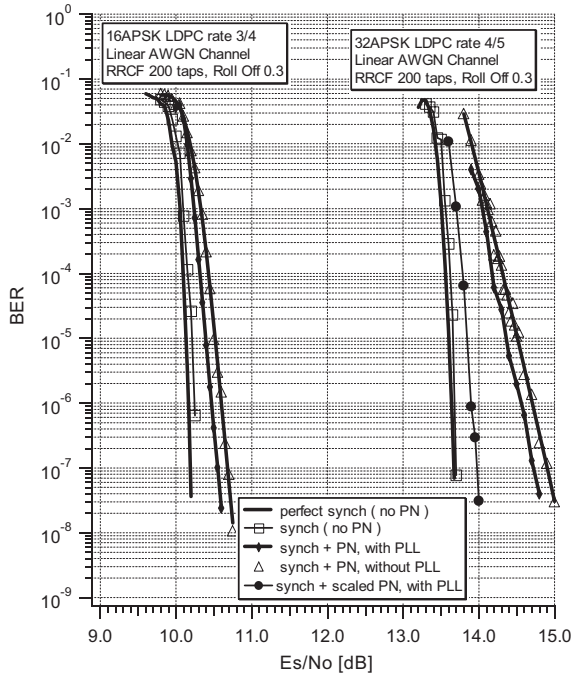


Figure 28. BER curves of 16APSK $r = \frac{3}{4}$ and 32APSK $r = \frac{4}{5}$ over an ideal linear channel and with the proposed carrier synchronization scheme in case of no phase noise or phase noise presence (nominal DVB-S2 mask and 3 dB scaled down version).

Numerical results show that the distance between pilot symbol fields has been optimized for QPSK and 8PSK constellations, thus some performance degradation is paid for higher order constellations requiring higher phase tracking accuracy. For these modulations, a shorter periodicity (given the same overhead) would have been more efficient but priority was given to the modulations that are expected to be more used in the near future for the DVB-S2 broadcast profile.

4.2. Impact of satellite channel

The simulations with the satellite channel have been performed according to the block diagram of Figure 1. The satellite channel included then IMUX, TWTA and OMUX. The optimal IBO was derived for each configuration. In all cases a SRRC filter roll-off factor of 0.3 has been adopted. For limiting the simulation length the total degradation has been computed at a working point corresponding to a bit error probability of 10^{-5} . For sake of completeness we report results for static, dynamic and optimized dynamic pre-compensation for each modulation scheme. The number of iterations for the dynamic pre-compensation has been optimized following the methodology described in Section 3.1. In the following plots we also reported the OBO corresponding to each pre-compensation scheme.

As expected, results for QPSK of Figure 29 show that the overall loss for the optimized dynamic pre-compensation amounts to 0.52 dB obtained at IBO = 0 dB. The results of

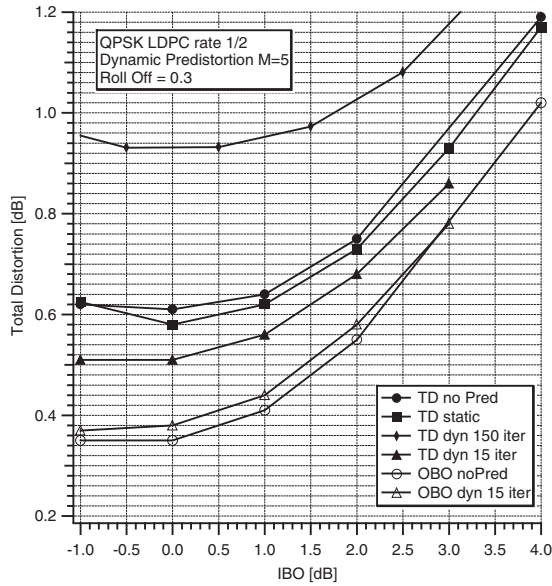


Figure 29. QPSK $r = \frac{1}{2}$ simulated performance: TD = total degradation D_{TOT} , OBO = output back-off. Dynamic pre-compensation optimized for $S = 15$ iterations.

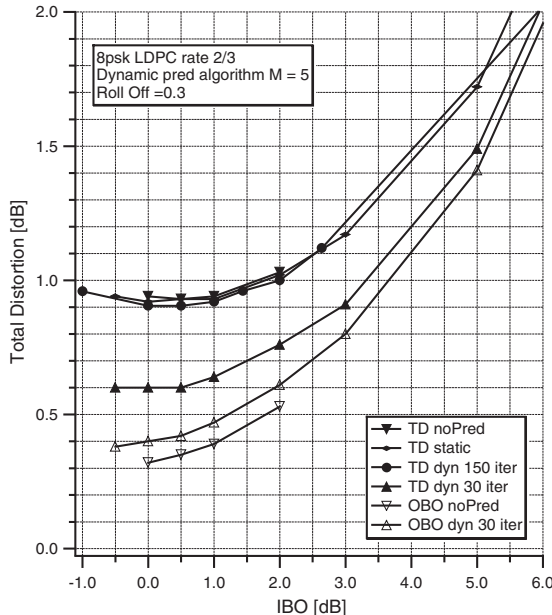


Figure 30. 8PSK $r = \frac{2}{3}$ simulated performance: TD = total degradation D_{TOT} , OBO = output back-off. Dynamic pre-compensation optimized for $S = 30$ iterations.

Figure 29 also indicate only 0.05 dB of gain using dynamic pre-distortion compared to static. However, not using the dynamic pre-compensation optimization scheme there will be a loss of 0.1 dB.

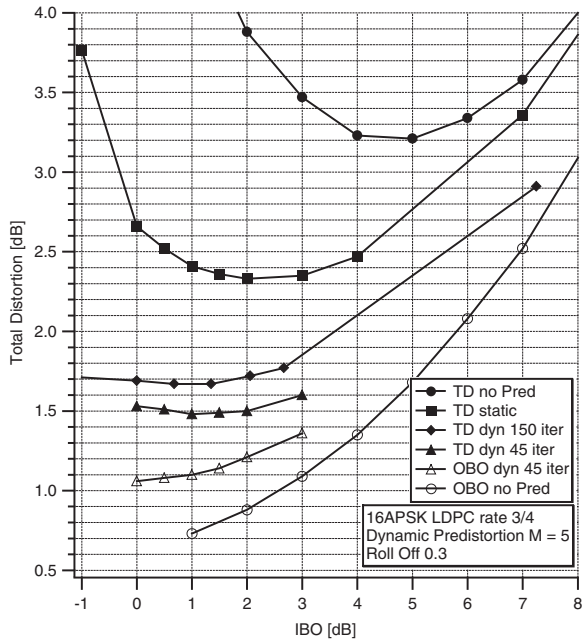


Figure 31. 16APSK $r = \frac{3}{4}$ simulated performance: TD = total degradation D_{TOT} , OBO = output back-off. Dynamic pre-compensation optimized for $S = 45$ iterations.

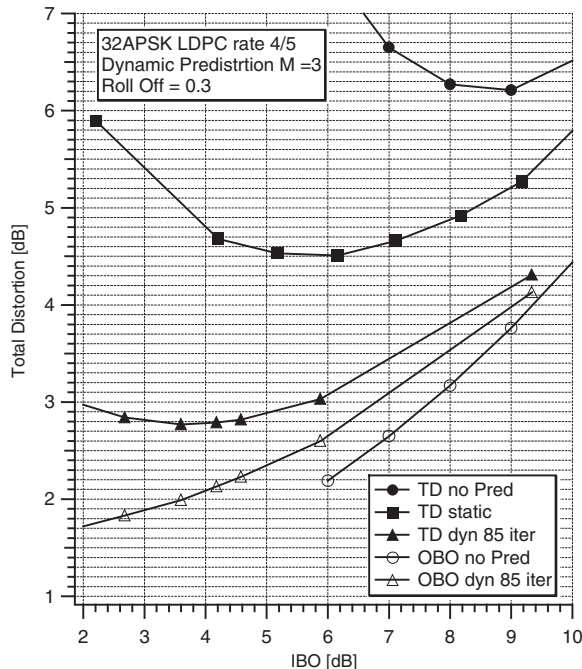


Figure 32. 32APSK $r = \frac{4}{5}$ simulated performance: TD = total degradation D_{TOT} , OBO = output back-off. Dynamic pre-compensation optimized for $S = 85$ iterations.

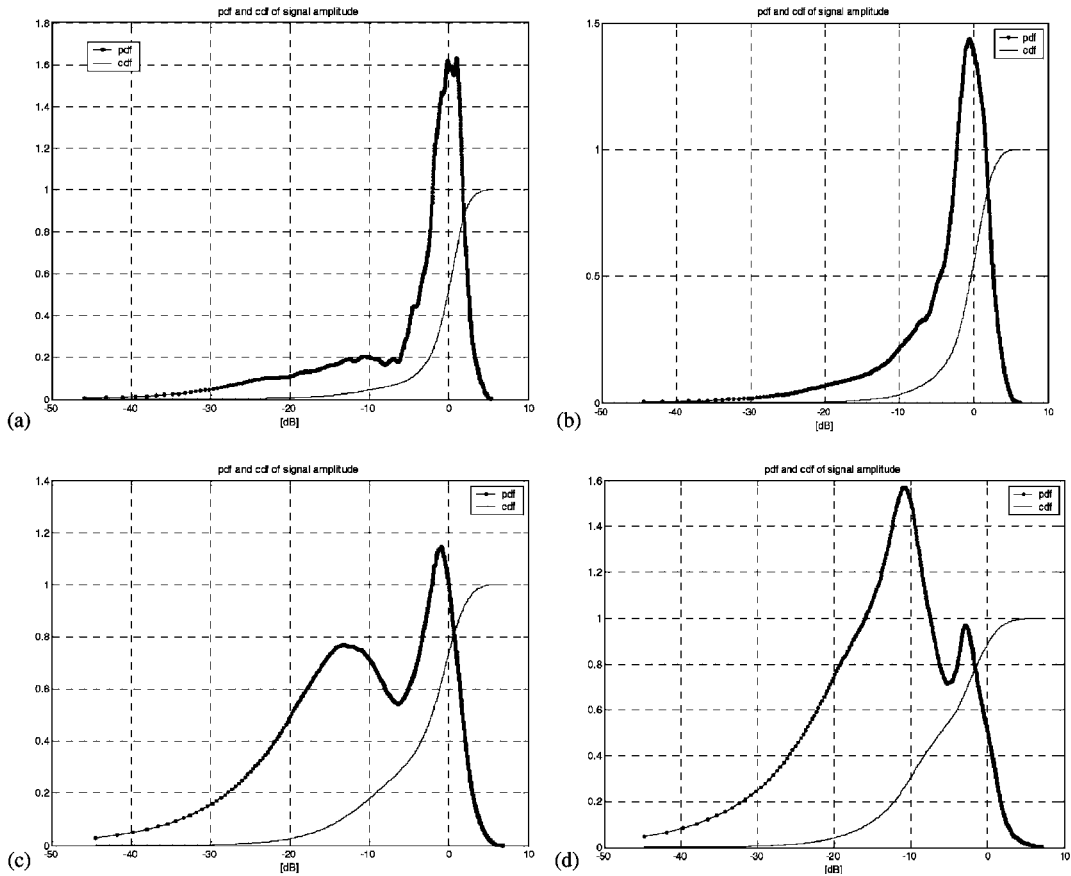


Figure 33. Simulated modulator signal envelope PDF with dynamic pre-compensation and SRRC with roll-off factor 0.3: (a) QPSK, (b) 8PSK, (c) 16APSK, (d) 32APSK.

In case of 8PSK, according to the results of Figure 30, the overall loss for the optimized dynamic pre-compensation amounts to 0.6 dB obtained at IBO = 0 dB. The optimized dynamic pre-compensation loss is 0.35 dB less than static pre-compensation and 0.35 dB compared to non-optimized dynamic pre-compensation ($S = 150$ iterations). Figure 31 reports the total distortion for 16APSK: for the optimized dynamic pre-distortion amounts to about 1.5 dB at IBO of 1 dB.

In case of 16APSK the advantage for exploiting dynamic pre-compensation amounts to about 0.8 dB compared to static pre-compensation while the dynamic optimization brings about 0.2 dB improvement. It is worth to notice that when the dynamic optimization scheme is implemented, the total distortion curve is rather flat for IBO smaller than 1 dB. Figure 32 reports the simulated total distortion results for 32APSK. For the optimized dynamic pre-distortion the total loss amounts to about 2.8 dB at IBO of 3.6 dB. In case of 32APSK the advantage for exploiting dynamic pre-compensation amounts to about 1.83 dB compared to static pre-compensation and about 3.44 dB compared to non-predistorted constellations.

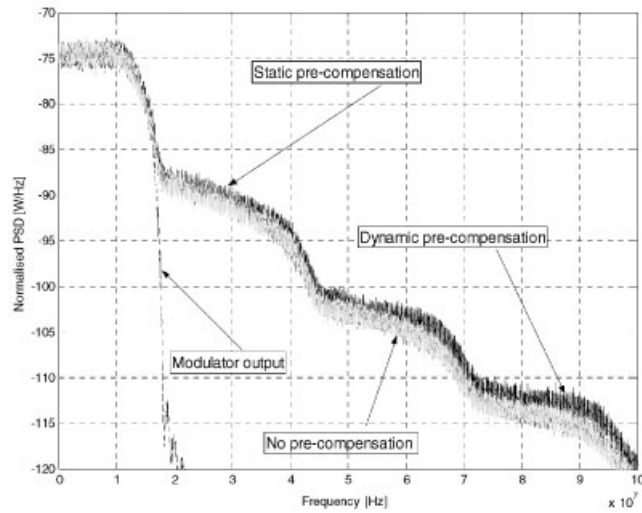


Figure 34. Comparison of the simulated PSD at the TWTA output (a) and at the OMUX output (b) for 16APSK without, with static and dynamic optimized pre-distortion. Dashed line represents the original APSK signal at the output of the modulator.

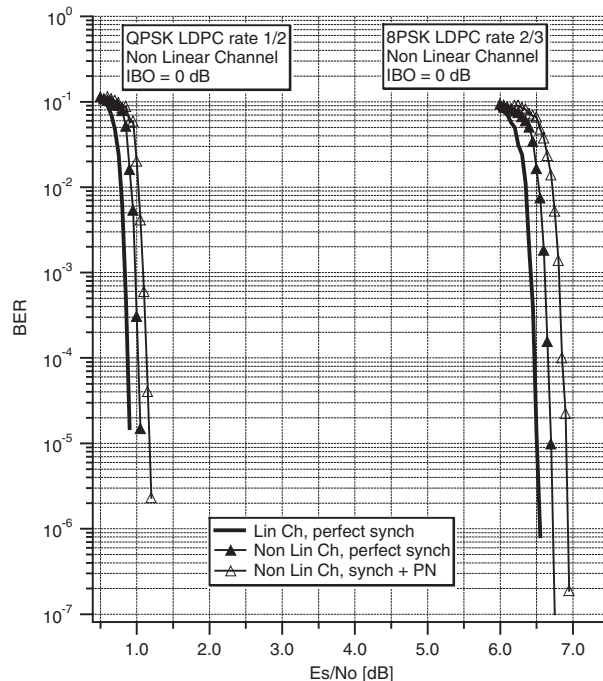


Figure 35. Comparison of BER curves for QPSK $r = \frac{1}{2}$ and 8PSK $r = \frac{2}{3}$ with ideal channel, non-linear channel and non-linear channel plus sync. loss (i.e. total loss).

It is also interesting to report the simulated probability density function (PDF) and cumulative distribution function (CDF) of the signal envelope at the modulator output for the optimized dynamic pre-compensation (see Figure 33). The corresponding simulated peak-to-average ratio is 5.4 dB for QPSK, 6.2 for 8PSK, 8.4 for 16APSK and 10.8 for 32APSK. Note that without the pre-dynamic optimization the peak-to-average ratio will be approximately the same for QPSK while will be higher by 4.5 and 4.4 dB for 8PSK and 16APSK, respectively.

It is interesting to observe in Figure 34 the impact of the various kinds of pre-compensation techniques on the power spectral density (PSD) of the APSK signal. It appears that the pre-distortion techniques impact on the PSD shape is minimal and is observable far away from the main lobe. Those high-frequency intermodulation components will be filtered out by the OMUX.

Figures 35 and 36 show the performance of the four modulation schemes with non-linear distortion and synchronization losses. Dynamic pre-compensation techniques are used with an IBO value that corresponds to the optimum. These results are also summarized in the efficiency- E_s/N_0 plane of Figure 37 where all the operating points of the four modulations over linear and non-linear channel and with and without synchronization losses are shown together with the relative modulation-constraint capacity bounds. The total loss Δ with respect to the ideal AWGN operating point is computed by subtracting the distances in dB to the capacity bound of the operating point with losses and the one for the ideal AWGN case. Results are also summarized in Table I. It is expected that over the non-linear channel for each modulation format the losses will slightly increase for higher coding rates being the FEC correction

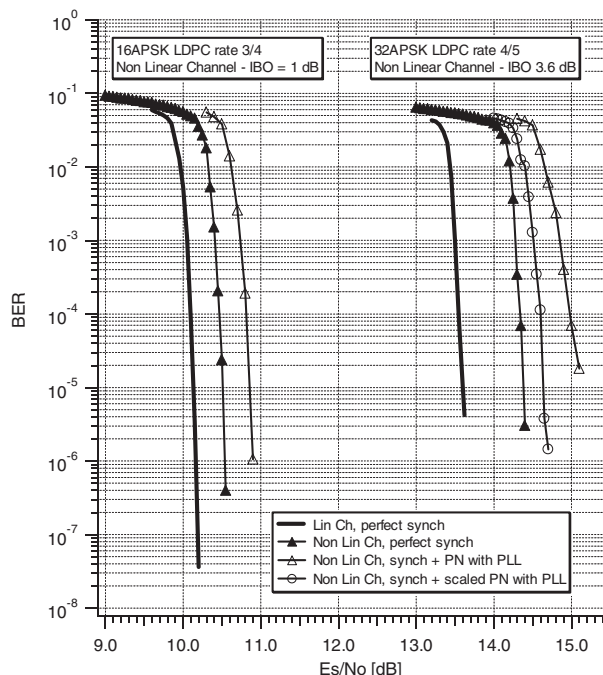


Figure 36. Comparison of BER curves for 16APSK $\frac{3}{4}$ and 32APSK with $r = \frac{4}{5}$ with ideal channel, non-linear channel and non-linear channel plus synch. loss (i.e. total loss).

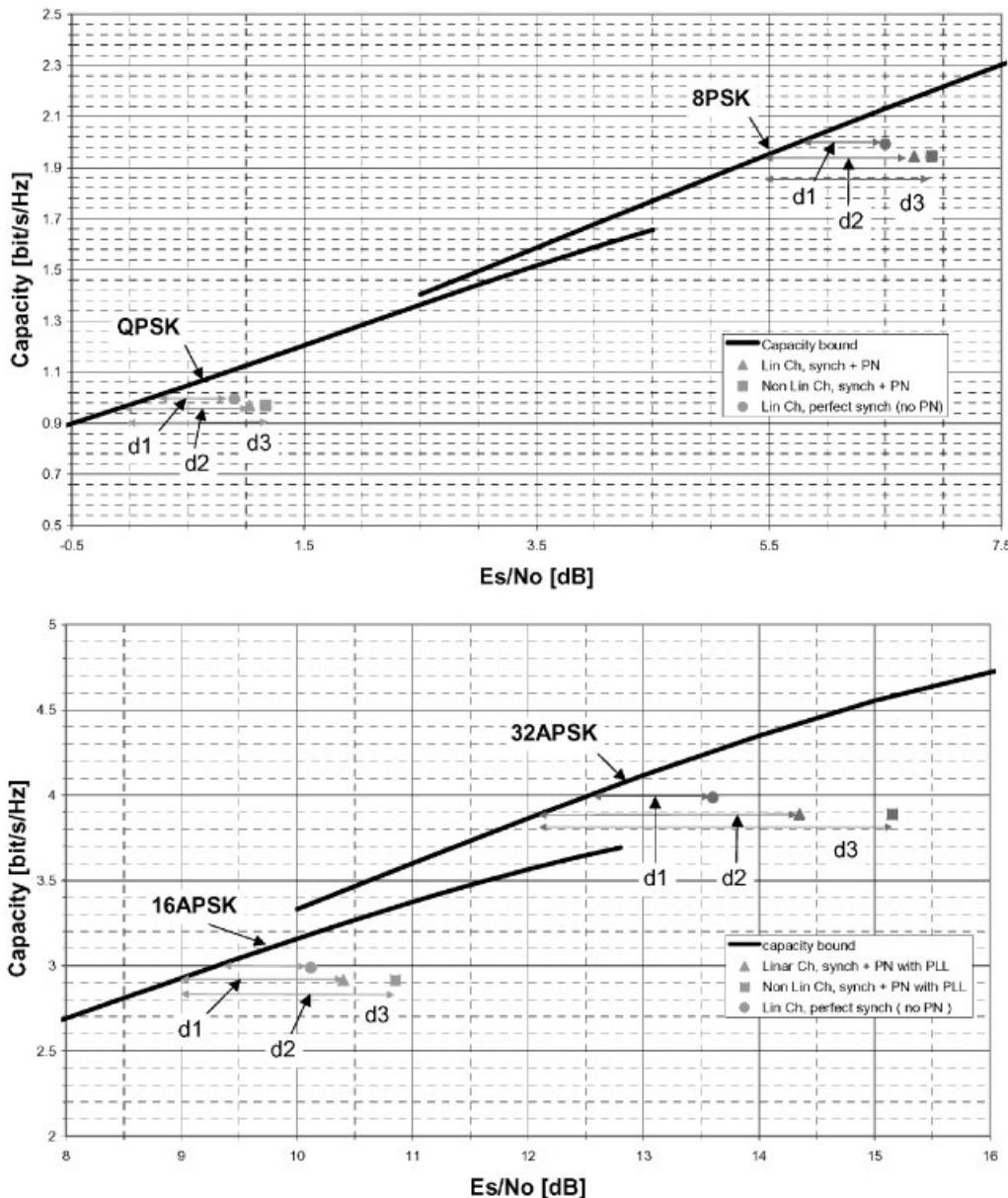


Figure 37. Efficiency versus E_s/N_0 plane showing the different operating points.

capabilities a bit less powerful and the higher operating SNR making the demodulator more sensitive to ISI. For linear channels instead, the losses, given a modulation alphabet, are expected to decrease with the coding rate as a result of an increased operating SNR, even though this effect will be partially offset by the higher FEC fragility.

Table I. Total losses of the four modulation schemes as derived from the efficiency/ E_s/N_0 plane.

	d_1 (dB)	d_2 (dB)	d_3 (dB)	Δ (dB)—linear channel with sync loss (d_2-d_1)	Δ (dB)—non-linear channel plus sync loss (d_3-d_1)
QPSK $\frac{1}{2}$	0.75	1.04	1.18	0.29	0.43
8PSK $\frac{2}{3}$	0.78	1.3	1.45	0.52	0.67
16APSK $\frac{3}{4}$	0.85	1.45	1.9	0.6	1.05
32APSK $\frac{4}{5}$	1.1	2.25	3.05	1.13	1.93

5. CONCLUSIONS

In this paper we presented a design of the main modulation/demodulation algorithms for a modem compliant with the DVB-S2 standard. The algorithms have been presented in detail and analysed by means of theory and computer simulations. In particular, non-linear channel pre-distortion algorithms have been studied and their performance investigated for all the modulation formats encompassed by the DVB-S2 standard. The optimum operating point (IBO) of the satellite non-linear TWTA power amplifier has been found for the given techniques. Results show that high-order modulation schemes up to 32APSK can be successfully used without excessive penalties.

Also, all the modem synchronization algorithms have been studied in great detail and their performance assessed also taking into account phase noise and non-linear satellite channel impact. The assumption is that pilots are used within the DVB-S2 physical layer frame, as this results in lower complexity algorithms with a very small overhead efficiency loss. In particular, the issue of carrier recovery (frequency and phase) is extensively analysed and some simple algorithms are presented which satisfy the DVB-S2 performance requirements with minor losses. End-to-end performance simulation results have been shown with all the designed modulation/demodulation algorithms active. Performance losses with respect to the ideal case are computed in the efficiency/ E_s/N_0 plane, showing very limited penalties with respect to the ideal case.

ACKNOWLEDGEMENTS

The authors would like to acknowledge Prof. Marco Luise and his team at the University of Pisa (Italy) for their valuable support on the development of the software simulation tool and on the implementation of the non-linear pre-distortion techniques.

REFERENCES

1. Reimers U, Morello A. DVB-S2, the second generation standard for satellite broadcasting and unicasting. *International Journal of Satellite Communications and Networking* 2004; **22**(3):249–268.
2. Morello A, Rinaldo R, Vazquez-Castro M. DVB-S2 ACM modes for IP and MPEG unicast applications. *International Journal of Satellite Communications and Networking* 2004; **22**(3):367–399.
3. De Gaudenzi R, Rinaldo R. Adaptive coding and modulation for next generation broadband multimedia systems. In *Proceedings of the 20th AIAA Satellite Communication Systems Conference*, Montreal, AIAA-Paper 2002-1863, May 2002.
4. Eroz M, Sun F-W, Lee L-N. DVB-S2 low density parity check codes with near Shannon limit performance. *International Journal on Satellite Communications and Networking* 2004; **22**(3):269–279.

5. Feher K. *Digital Communications—Satellite/Earth Station Engineering*. Prentice-Hall Inc.: Englewood Cliffs, New Jersey, U.S.A., 1983.
6. Cominetti M, Morello A. Digital video broadcasting over satellite (DVB-S): a system for broadcasting and contribution applications. *International Journal on Satellite Communication* 2000; **18**:393–410.
7. Mengali U, D'Andrea AN. *Synchronization Techniques for Digital Receivers*. Plenum Press: New York, U.S.A., 1997.
8. ETSI EN 302 307 V1.1.1 (2004-01) European Standard (Telecommunications series) Digital Video Broadcasting (DVB) Second generation framing structure, channel coding and modulation systems for Broadcasting, Interactive Services, News Gathering and other broadband satellite applications.
9. De Gaudenzi R, Guillen i Fabregas A, Martinez Vicente A. Turbo-coded APSK modulations for satellite broadcasting and multicasting—Part I: coded modulation design. *IEEE Transactions on Wireless Communications* 2003; submitted.
10. De Gaudenzi R, Luise M. Design and analysis of an all-digital demodulator for trellis coded 16-QAM transmission over a nonlinear satellite channel. *IEEE Transactions on Communications* 1995; **43**(2/3/4) part I:659–688.
11. De Gaudenzi R, Guillen i Fabregas A, Martinez Vicente A. Turbo-coded APSK modulations for satellite broadcasting—Part II: end-to-end performance. *IEEE Transactions on Wireless Communications* 2003; submitted.
12. Karam G, Sari H. A data pre-distortion technique with memory for QAM radio systems. *IEEE Transactions on Communications* 1991; **COM-39**(2):336–344.
13. Gardner FM. A BPSK/QPSK timing-error detector for sampled receivers. *IEEE Transactions on Communications* 1986; **COM-34**(5):423–429.
14. Sun F-W, Jiang Y, Lee L-N. Frame synchronization and pilot structure for DVB-S2. *International Journal of Satellite Communications and Networking* 2004; **22**(3):319–339.
15. Luise M, Reggiannini R. Carrier frequency recovery in all digital modems for burst mode transmissions. *IEEE Transactions on Communications* 1995; **COM-43**:1169–1178.
16. Oerder M, Meyr H. Digital filter and square timing recovery. *IEEE Transactions on Communications* 1988; **COM-36**: 605–612.